

Effect of Angle of Attack on Propeller Aeroacoustics at Positive and Negative Thrust

Goyal, Jatinder; Sinnige, Tomas; Ferreira, Carlos; Avallone, Francesco

DOL

10.2514/1.c038073

Publication date 2025

Published in Journal of Aircraft

Citation (APA)

Goyal, J., Sinnige, T., Ferreira, C., & Avallone, F. (2025). Effect of Angle of Attack on Propeller Aeroacoustics at Positive and Negative Thrust. *Journal of Aircraft*, *62*(5), 1130-1150. https://doi.org/10.2514/1.c038073

Important note

To cite this publication, please use the final published version (if applicable). Please check the document version above.

Copyright

Other than for strictly personal use, it is not permitted to download, forward or distribute the text or part of it, without the consent of the author(s) and/or copyright holder(s), unless the work is under an open content license such as Creative Commons.

Takedown policy

Please contact us and provide details if you believe this document breaches copyrights. We will remove access to the work immediately and investigate your claim.

Green Open Access added to <u>TU Delft Institutional Repository</u> as part of the Taverne amendment.

More information about this copyright law amendment can be found at https://www.openaccess.nl.

Otherwise as indicated in the copyright section: the publisher is the copyright holder of this work and the author uses the Dutch legislation to make this work public.



Effect of Angle of Attack on Propeller Aeroacoustics at Positive and Negative Thrust

Jatinder Goyal,* Tomas Sinnige,† and Carlos Ferreira‡

Delft University of Technology, 2629 HS Delft, The Netherlands
and

Francesco Avallone[§]
Polytechnic University of Turin, 10129 Torino, Italy
https://doi.org/10.2514/1.C038073

Conventional propellers operating at negative thrust conditions, even at 0 deg angle of attack, are characterized by flow separation and significantly different noise emissions than at positive thrust conditions. Operating the propeller at nonzero angles of attack at negative thrust conditions can further impact aerodynamic performance and far-field noise emission. This paper studies these effects using lattice-Boltzmann very large eddy simulations coupled with the Ffowcs Williams and Hawkings analogy. At positive thrust, operation at 10 deg angle of attack increases thrust along the freestream direction by approximately 3% compared to operation at 0 deg angle of attack, while efficiency remains constant. Conversely, the negative thrust condition shows approximately a 7% decrease in thrust magnitude and a 10% reduction in regenerated power. In this condition, the positively cambered blade sections exhibit dynamic stall, resulting in broadband fluctuations of up to 10% of the mean loading near the blade tip. The nonzero angle of attack induces opposite variations in absolute blade loading between positive and negative thrust conditions, resulting in opposite changes in the noise directivity. At positive thrust, noise increases in the region from which the propeller is tilted away (i.e., below the propeller at a positive angle of attack), while the

opposite occurs at negative thrust. The varying blade loading over the azimuth results in destructive interference between loading and thickness noise for the negative thrust case at the 10 deg angle of attack. These findings highlight the crucial role of considering nonzero angles of attack in propeller design and optimization analyses.

Nomenclature									
\boldsymbol{B}	=	number of propeller blades							
BPF	=	blade passing frequency; $B \cdot n$, Hz							
C_P	=	propeller power coefficient; $P/\rho_{\infty}n^3D_p^5$ propeller thrust coefficient; $T/\rho_{\infty}n^2D_p^4$							
C_T	=	propeller thrust coefficient; $T/\rho_{\infty}n^2D_p^4$							
c	=	section chord, m							
c_o	=	speed of sound in dry air at 15°C, m/s							
c_p	=	sectional pressure coefficient based on local dynamic							
		pressure; $(p - p_{\infty})/0.5\rho_{\infty}((V_{\infty}\cos\alpha_{\infty})^2 + (\Omega r +$							
		$V_{\infty} \sin \alpha_{\infty} \sin \phi)^2$							
D_p	=	propeller diameter, m							
F_N	=	force in the normal direction (Z axis), N							
F_{Y}	=	force in the side direction (Y axis), N							
f	=	frequency, Hz							
J	=	propeller advance ratio; V_{∞}/nD_p							
$M_{ m ht}$	=	helicoidal tip rotational Mach number; $\sqrt{M_{\infty}^2 + M_{\rm tip}^2}$							
M_{tip}	=	tip rotational Mach number; $\Omega R/c_0$							
M_{∞}	=	freestream Mach number							
N_C	=	normal force coefficient based on freestream dynamic							
		pressure; $F_N/\rho_\infty V_\infty^2 D_p^2$							
n	=	propeller rotation speed, Hz							
OSPL	=	overall sound pressure level, dB							
\boldsymbol{P}	=	propeller power, W							
		as Paper 2023-3217 at the 2023 AIAA Aviation Forum, San							

Presented as Paper 2023-3217 at the 2023 AIAA Aviation Forum, San Diego, CA, June 12–16, 2023; received 24 May 2024; accepted for publication 5 January 2025; published online 10 March 2025. Copyright © 2025 by J. Goyal, T. Sinnige, C. Ferreira, and F. Avallone. Published by the American Institute of Aeronautics and Astronautics, Inc., with permission. All requests for copying and permission to reprint should be submitted to CCC at www.copyright.com; employ the eISSN 1533-3868 to initiate your request. See also AIAA Rights and Permissions www.aiaa.org/randp.

*Ph.D. Candidate, Wind Energy Section, Faculty of Aerospace Engineering, Kluyverweg 1; J.Goyal@tudelft.nl.

[†]Assistant Professor, Flight Performance and Propulsion Section, Faculty of Aerospace Engineering, Kluyverweg 1; T.Sinnige@tudelft.nl.

[‡]Full Professor, Wind Energy Section, Faculty of Aerospace Engineering, Kluyverweg 1; C.J.SimaoFerreira@tudelft.nl.

§Full Professor, Department of Mechanical and Aerospace Engineering, Corso Duca degli Abruzzi 24; francesco.avallone@polito.it.

PSD	_	nower	spectrum	density	dR/H ₂

 P_C = propeller power coefficient based on freestream

dynamic pressure; $P/\rho_{\infty}V_{\infty}^{3}D_{p}^{2}$ p = static pressure, Pa

 p_{ref} = reference sound pressure, Pa

R = propeller radius, m

 Re_c = Reynolds number based on chord of the propeller

blade; $\rho_{\infty} V_{\text{eff}} c / \mu_{\infty}$ = radial coordinate, m

T = propeller thrust, N

= propeller thrust coefficient based on freestream

dynamic pressure; $T/\rho_{\infty}V_{\infty}^2D_p^2$ T_c' = sectional thrust coefficient based on freestream

dynamic pressure; $T'/\rho_{\infty}V_{\infty}^{2}D_{p}$

= section thickness, m

 V_{eff} = sectional effective velocity; $\sqrt{V_{\infty}^2 + (\Omega r)^2}$, m/s

 V_{∞} = freestream velocity, m/s

X = axial coordinate, m

Y = horizontal axis in the plane of propeller rotation, m

 Y_C = side force coefficient based on freestream dynamic

pressure; $F_Y/\rho_{\infty}V_{\infty}^2D_p^2$

Z = vertical axis in the plane of propeller rotation, m

 α = angle of attack, deg

 $\beta_{0.7R}$ = blade pitch angle at 70% of the radius, deg

 $\Delta J' = \text{change in local advance ratio due to in-plane velocity component; } (V_{\infty} \cos \alpha_{\infty} / (n + (V_{\infty} \sin \alpha_{\infty} \sin \phi /$

 $(2\pi r)D_p - J$

 $\Delta \alpha_{g_r}$ = change in local geometric angle of attack due to in-plane velocity component at the blade section located at r

 $\Delta_{\alpha_{\infty}}$ = relative change in performance parameter at nonzero

 α_{∞} compared to $\alpha_{\infty} = 0$ deg = phase delay: $\tan^{-1}(Y_C/N_C)$, def

 $\Delta \phi$ = phase delay; $\tan^{-1}(Y_C/N_C)$, deg η_p = propeller efficiency; TV_{∞}/P η_t = turbine efficiency; P/TV_{∞}

 $\eta_t = \text{turbine efficiency; } P/IV_{\infty}$ $\theta = \text{axial directivity angle, deg}$

 μ = dynamic viscosity of dry air at 15°C, (N·s)/m²

 ρ = air density, kg/m³ σ = standard deviation

 σ = standard deviation ϕ = azimuthal position, deg

 Ω = rotational speed; $2\pi n$, rad/s

Subscripts/Superscripts

/ = per unit span ∞ = freestream

I. Introduction

THE increasing need for sustainable aviation has spurred the development of innovative technologies. Fuel cells, hydrogen combustion, and electric architectures are a few examples of innovative technologies to store/deliver energy during flight. These technologies are often coupled with propellers for thrust generation due to their high propulsive efficiency up to moderate Mach number and at low cruise altitudes [1]. When coupled with electric motors, propellers enable novel configurations such as distributed propulsion, tip-mounted propellers, boundary-layer ingesting propellers, and so on. Furthermore, electric motors allow propellers to operate at negative thrust conditions, leading to benefits such as steeper descent, reduced landing run, better maneuverability [2,3], lower community noise [4], and energy regeneration [5,6].

Despite these promising features, only a few studies have focused on propellers operating in the negative thrust regime. The existing studies primarily focus on isolated propellers in uniform inflow conditions [7–10], which do not represent the complex flow conditions experienced by propellers mounted on a real aircraft. Though Sinnige et al. [11,12] studied wing-tip mounted propellers operating at negative thrust, their focus was on system-level performance, and the work did not evaluate the effect of nonzero angle of attack (angle between the propeller axis and freestream velocity) and the airframe installation on the propeller performance.

Even in uniform inflow conditions, the operation of conventional propellers at negative thrust conditions leads to flow separation around the blades [7,9-11]. The flow separation is likely to be further amplified when operating at a nonzero angle of attack (AOA). The periodic perturbations in the inflow conditions due to the operation at a nonzero AOA are hypothesized to potentially result in periodic stall of the blade sections, impacting both aerodynamic and aeroacoustic performance. Understanding such effects is crucial for designing propellers that optimize energy regeneration while minimizing noise emissions. To address this knowledge gap, this study investigates the effect of a nonzero AOA on the aerodynamic and aeroacoustic performance of a propeller operating at negative thrust compared to positive thrust. To isolate the effects of nonzero AOA on propeller performance, this study focuses solely on the isolated propeller and does not consider the additional complexities introduced by its installation on an aircraft.

This study employs lattice-Boltzmann (LB) very large-eddy simulations (VLES) coupled with the Ffwocs Williams and Hawkings (FWH) integral solution based on Farassat's formulation 1A [13]. The analysis focuses on the changes in the integrated propeller performance, blade loading, loading fluctuations, and propeller

slipstream to understand the differences in the aerodynamic performance at 0 deg and nonzero AOA. Furthermore, the changes in the aeroacoustic performance are characterized by comparing the far-field noise at 0 deg and nonzero AOA.

II. Methodology

This section establishes the methodological framework employed in the study. The computational setup of LB–VLES simulations, including the details of domain size, boundary conditions, and grid dependence study, is described first. The computational setup is followed by the description of the propeller geometry used in this study, along with the details of the reference experimental setup used to validate the numerical setup. Subsequently, the operating conditions used for validation of the setup and further analysis are listed. Finally, to ensure clarity and consistency throughout the paper, the key conventions used in this study are defined.

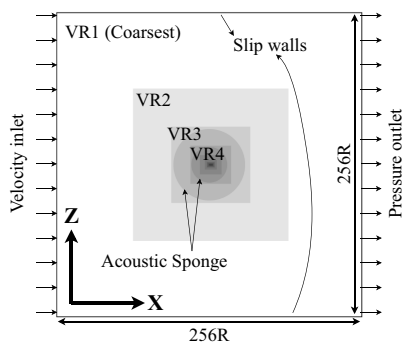
A. Computational Setup

LB-VLES simulations were chosen for this study because of their proven effectiveness in similar applications [14,15] and low dissipation and dispersion properties [16,17], ideal for aeroacoustic studies. A detailed description of the lattice-Boltzmann method can be found in the work by Succi [18] and Shan et al. [19]. The LB-VLES equations were solved using SIMULIA® PowerFLOW 6-2021-R6, a commercially available solver.

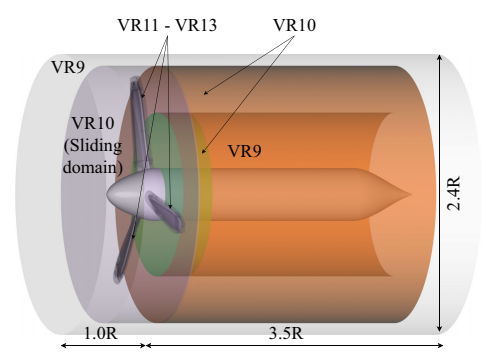
1. Computational Volume and Boundary Conditions

The computational domain was a cube with a domain size of 128D; see Fig. 1a. Such a large domain size was motivated by the interest in aeroacoustics. The domain was discretized using a Cartesian mesh, employing 19 discrete velocities in three dimensions (D3Q19), including a third-order truncation of the Chapman–Enskog expansion. PowerFLOW uses an explicit time integration approach to solve the equations with a Courant–Friedrichs–Lewy number of 1 to maintain numerical stability. The particle distribution within the domain is determined using a collision term based on a unique Galilean invariant [20], and the equilibrium distribution follows the Maxwell–Boltzmann distribution [21]. PowerFLOW uses a VLES model to account for the effects of subgrid unresolved turbulence scales. This model relies on the $k-\epsilon$ renormalization equations [22] to predict the turbulent relaxation time.

The boundaries of the domain were specified as a velocity inlet, a pressure outlet, and slip walls. The angle of attack was varied by rotating the inlet velocity around the Y axis. The large domain size ensured a uniform total pressure profile at the inlet and minimized the influence of boundary conditions on the simulation results. Noslip conditions were applied to the propeller blades, spinner, and nacelle. The no-slip boundary condition on walls in PowerFLOW is approximated using a pressure-gradient extended wall model [23,24]. This model extends the generalized law-of-the-wall model



a) Full computational domain



b) Zoomed view of domain showing the distribution of VR regions near the propeller

Fig. 1 Computational domain and boundary conditions along with the variable resolution (VR) regions.

[25] to consider the impact of pressure gradients on boundary-layer development.

For the sliding mesh, a volume of revolution was defined around the propeller blades and spinner; see Fig. 1b. In the radial direction, a clearance of 0.1R was defined between the blade tip and the outer edge of the rotating domain. Similarly, in the axial direction, a clearance of 0.05R was defined between the spinner edge and the edge of the rotating domain. In total, 13 variable resolution (VR) regions were employed for LB-VLES simulations, based on the work of Avallone et al. [26]. The cell volume changes by a factor of 8 between different VR regions. The finest three VR regions (VR13-11) were employed around the propeller blades as marked in Fig. 1b. VR10 was used in the sliding domain and downstream up to a distance of 0.5R from the propeller. Farther downstream, a hollow cylinder with VR10 resolution was used to capture the strong gradients associated with tip vortices. VR9 was used in a cylinder with a radius of 1.2R encompassing the propeller blades, spinner, and blade, extending 1R upstream and 3.5R downstream of the propeller.

Because of the interest in aeroacoustics, VR regions 1–8 were used to ensure domain size sufficiency to minimize acoustic reflections. Further, an acoustic sponge was used to absorb any remaining acoustic reflections coming from the boundaries by exponentially varying the kinematic viscosity per unit temperature from $0.005 \text{ m}^2/(\text{sK})$ at 15R up to $0.5 \text{ m}^2/(\text{sK})$ at 30R as shown in Fig. 1a. The acoustic sponge started at a distance of 15R from the propeller, ensuring minimal impact on the aerodynamic results.

2. Far-Field Noise Computation

The study adopted a hybrid computational fluid dynamics (CFD)/CAA (computational aeroacoustics) approach to compute far-field noise, mitigating computational costs associated with acoustic wave propagation. The FWH analogy was solved based on the forward-time solution [27] of Farassat's formulation 1A [13] using the postprocessing software SIMULIA® PowerACOUSTIC. This formulation includes surface integral terms, that is, acoustic monopoles (thickness noise) and dipoles (loading noise). The volume integral, that is, quadrupole term, is neglected in this formulation, which accounts for the nonlinear effects in the volume surrounding the integration surface. The quadrupole term was assumed to be negligible for the operating conditions considered in this study as the convective Mach number of the propeller wake is less than 0.30 [28].

The far-field noise was computed on a circular array with a radius of 10D, centered around the propeller center, with 24 evenly spaced virtual microphones in two planes: the plane of propeller rotation and the plane along the axis of the propeller.

3. Grid Dependence Study

To ensure consistency between simulations, the nonzero angle of attack (AOA) cases use the same grid resolution employed for the

0 deg AOA case. A detailed grid dependence study of LB–VLES simulations at 0 deg AOA can be found in the authors' previous work [10]. Five different grids were evaluated for the grid dependence study with fine equivalent voxels varying from 1 million to 100 million. Based on the grid dependence study, the grid with fine equivalent voxels of 62 million, corresponding to a resolution of 304, was chosen for the present study. The resolution is defined as the number of voxels per characteristic length, which in this case is the chord length at 0.7R blade span (approximately 31 mm). The chosen grid resulted in a $y^+ > 15$ over the blade surface. The impact of this y^+ value has been quantified in the authors' previous work [29].

4. Simulation Run Time

The simulations were run for 10 revolutions in total, out of which the last eight revolutions were used for the analysis after ensuring that the transient period was over. The simulations at 0 deg and nonzero AOA were initiated using the converged solution of a coarser mesh.

B. Propeller Geometry and Reference Experimental Setup

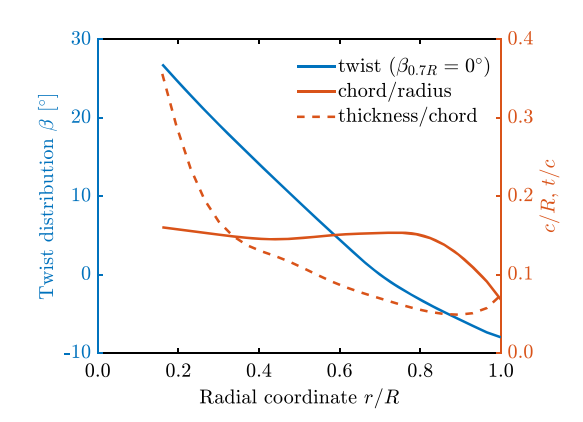
The propeller investigated in this study is the TUD-XPROP, a scaled version of a propeller for a previous-generation regional turboprop aircraft. This propeller was used in the previous work at 0 deg AOA [10,29]. The propeller has a diameter of 0.4064 m and a hub diameter of 0.092 m. The nacelle of the propeller extends up to approximately 1.6D downstream. Originally, the propeller had six blades; however, only three blades were used in the experiment due to limitations of the power dissipation system when operating at negative thrust [8,9]. The propeller can be seen in Fig. 2a along with its geometry parameters in Fig. 2b.

To validate the LB-VLES simulations, comparisons are made with the experimental load cell data available from the work of Nederlof et al. [9]. The experiments were conducted at a freestream Mach number of 0.09, with the helicoidal tip Mach number ranging from 0.21 to 0.51. Because the tip Mach number is lower than in real-world scenarios, the absolute noise levels obtained in this study are expected to be lower in magnitude than those experienced in actual operation. As the TUD-XPROP is a scaled-down model, the Reynolds number, based on the chord of the blade sections of the propeller, is an order of magnitude lower than in full-scale flights. Operating the propeller at these lower Reynolds numbers in the experiments led to an increased susceptibility to flow separation and the presence of separation bubbles on the propeller blades [10]. This made it harder to match the numerical predictions with the experimental data as the prediction of separation bubble size and reattachment location is sensitive to various parameters such as the resolution of the boundary layer y^+ , incoming turbulence, surface roughness, and subgrid-scale modeling [30-33].

The experimental data used in the present paper were corrected for wind-tunnel boundary interference. Three specific corrections were applied to correct the freestream velocity as shown in Eq. (1) based on



a) Isolated propeller with three blades installed on a sting



b) Propeller blade geometry

Fig. 2 Propeller setup in the wind tunnel and geometry.

Table 1 Wind-tunnel boundary interference corrections

Thrust condition	J	$\epsilon_{ m nacelle}$	$\epsilon_{ m sting}$	$\epsilon_{ m slipstream}$	$\epsilon_{ m total}$
Positive thrust	0.60	0.0011	0.0035	[-0.0047 -0.0038]	[-0.0002 +0.0008]
Negative thrust	1.10	0.0011	0.0035	[+0.0023 +0.0031]	[+0.0069 +0.0077]

the work by Barlow et al. [34]: 1) solid blockage due to the nacelle $\epsilon_{\rm nacelle}$, 2) solid and wake blockage due to the support structure $\epsilon_{\rm sting}$, and 3) propeller slipstream blockage $\epsilon_{\rm slipstream}$. Table 1 lists the value of these corrections for the operating conditions considered in this study as explained next in Sec. II.C. The $\epsilon_{\rm nacelle}$ and $\epsilon_{\rm sting}$ depend upon the geometrical factors and are not affected by the chosen operating condition. In contrast, the propeller slipstream blockage is directly proportional to the thrust coefficient T_C and therefore varies with the chosen operating condition. For the positive thrust case (J=0.60), the propeller slipstream blockage cancels the effects induced by the blockage due to nacelle and sting. In contrast, the blockage effects add up for the negative thrust case (J=1.10):

$$V_{\text{corrected}} = V_{\text{uncorrected}}(1 + \epsilon_{\text{total}})$$
 (1)

$$\epsilon_{\text{total}} = \epsilon_{\text{nacelle}} + \epsilon_{\text{sting}} + \epsilon_{\text{slipstream}}$$
 (2)

Symmetric polynomial fits around the 0 deg AOA were employed to develop reduced-order response models for thrust, power, side force, and normal force coefficients (T_C , P_C , Y_C , and N_C , respectively) using the corrected experimental data. The initial polynomial orders were determined by minimizing the root mean square errors. Subsequently, terms with a greater than 5% probability of having a nonzero coefficient due to random error were removed to obtain a reduced-order response model [35].

C. Operating Conditions

The operating conditions for the simulations were chosen to ensure both validation against existing experimental data [8,9] and comprehensive analysis of the aerodynamic and aeroacoustic characteristics of the propeller. For this purpose, two advance ratios (J=0.60 and 1.10) and two AOA (0 deg and 10 deg) were chosen as detailed in Table 2.

The first advance ratio, J=0.60, represents a positive thrust condition with moderate thrust ($T_C\approx 0.12$). Although the corresponding pitch angle is not optimal for the positive thrust regime and leads to trailing-edge separation [7], it serves as a valuable baseline for evaluating the changes in the aerodynamic and aero-acoustic performance of the propeller operating at the positive thrust with the change in the AOA.

The second advance ratio, J=1.10, represents a negative thrust condition achieved by reducing the rotational speed of the propeller as compared to the positive thrust condition. In this way, the angle of attack to the blade sections is decreased to a negative value, leading to negative thrust. This choice was primarily motivated by the availability of experimental data for validation. This condition has been used to evaluate the effect of nonzero AOA on the aerodynamic and aeroacoustic performance of the propeller at negative thrust compared to the operation at 0 deg AOA.

D. Physical Mechanisms and Reference Frames for Operation of a Propeller at Nonzero ${\bf AOA}$

To establish the conventions used in this study, it is imperative to understand the underlying physical mechanisms when the propeller operates at a nonzero AOA. Therefore, these physical mechanisms are described in this section, along with the definition of reference frames used in this study.

1. Azimuthal Position

When the propeller operates at a nonzero AOA, the incoming flow no longer aligns with the propeller axis. This misalignment results in a varying propeller blade performance with the azimuthal position. The convention for the phase angle ϕ defining the azimuthal position of the blade is illustrated in Fig. 3.

2. Local Advance Ratio

The in-plane velocity resulting from the nonzero AOA induces a variation in the local advance ratio for each blade section during the rotation, as shown in Fig. 4. The propeller blade on the advancing side (downward direction, $\phi = 90$ deg) experiences a higher inplane velocity, leading to a reduced local advance ratio compared to the uniform inflow. Conversely, the propeller blade on the retreating side (upward direction, $\phi = 270$ deg) experiences a lower in-plane velocity, resulting in an increased local advance ratio. This variation is particularly pronounced in the negative thrust condition (J = 1.10) due to its higher baseline advance ratio, as evident in Fig. 4b.

The local advance ratio directly influences the local geometric AOA at each blade section for a given pitch and twist distribution. A higher local advance ratio (on the retreating side) reduces the local geometric AOA compared to uniform inflow and vice versa. Consequently, the most significant changes in the local geometric AOA occur at the blade root, with the highest increase at $\phi = 90\,$ deg (advancing side) and the highest decrease at $\phi = 270\,$ deg (retreating side); see Fig. 4.

3. In-Plane Force and Delayed Aerodynamic Response

The variations in local J result in varying thrust and tangential forces over the rotation. The differences in the tangential force on the advancing and retreating sides result in an in-plane force. This in-plane force acts at a delayed $\Delta\phi$ with respect to $\phi=90$ deg. This delay is a consequence of the sinusoidal variation in the local inflow conditions at blade sections over the rotation, similar to the delay of the forces observed on an airfoil subjected to an unsteady inflow [36]. Because of this aerodynamic delay, the in-plane force can be decomposed into normal N_C and side forces Y_C , which relate to $\Delta\phi$ as per Eq. (3). Here, the normal force is considered positive in the direction of $\phi=0$ deg, and the side force is considered positive in the direction of $\phi=90$ deg as shown in Fig. 5:

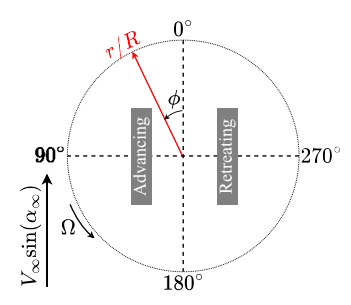
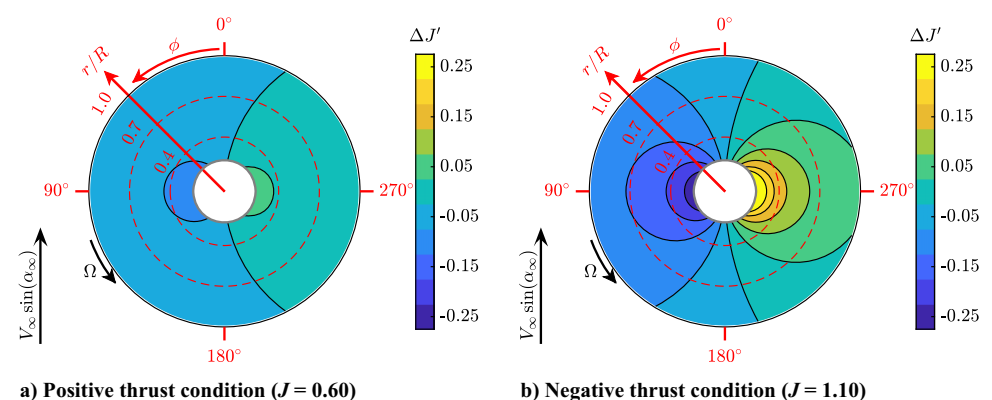


Fig. 3 Definition of phase angle ϕ and conventions used in this study.

Table 2 Operating conditions used for the validation and analysis

Thrust condition	J	α_{∞} , deg	$\beta_{0.7R}$, deg	M_{∞}	n, Hz	$M_{ m ht}$	Max Re_c
Positive thrust	0.60	0 deg, 10 deg	15 deg	0.09	123.03	0.47	3.5×10^{5}
Negative thrust	1.10	0 deg, 10 deg	15 deg	0.09	67.11	0.27	2.0×10^5



a) Positive thrust condition (J = 0.60)

Fig. 4 Change in the local advance ratio over a rotation at 10 deg angle of attack compared to 0 deg angle of attack.



Fig. 5 Convention for normal N_C and side forces Y_C .

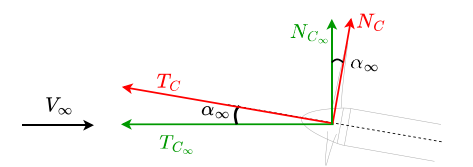


Fig. 6 Components of propeller performance parameters in propeller axis aligned and freestream aligned reference frames.

$$\Delta \phi = \tan^{-1} \left(\frac{Y_C}{N_C} \right) \tag{3}$$

4. Freestream-Aligned Performance Parameters

The performance parameters projected along the propeller axis are crucial for understanding the isolated propeller performance, while the performance parameters projected along the freestream direction are relevant for the performance of the system at the aircraft level. Therefore, two types of definitions are used for comparing the propeller performance parameters: 1) aligned with the propeller axis and 2) aligned with the freestream ∞ . The parameters aligned with the freestream, derived from those aligned with the propeller axis, are illustrated in Fig. 6 and defined by Eqs. (4–6):

$$T_C = T_C \cos \alpha_\infty - N_C \sin \alpha_\infty \tag{4}$$

$$N_{C_{\infty}} = N_C \cos \alpha_{\infty} + T_C \sin \alpha_{\infty} \tag{5}$$

$$\eta_{p_{\infty}} = \frac{T_{C_{\infty}}}{P_{C}} \tag{6}$$

Comparison of Simulated Propeller Performance with Experimental Data

Tables 3 and 4 present a comparison of simulated and measured (experimental) propeller performance parameters for both positive (J = 0.60) and negative thrust conditions (J = 1.10). These tables also report the experimental uncertainties calculated for a 95% confidence interval. Moreover, they present the key performance parameters at both 0 and 10 deg angles of attack, along with the

Propeller performance in the positive thrust condition (J = 0.60) at 0 deg and 10 deg angles of attack

Method	α_{∞} , deg	T_C	P_C	η_p	$T_{C_{\infty}}$	η_{p_∞}	Y_C	N_C	$N_{C_{\infty}}$	$\Delta \phi$, deg
Experiment	0 deg	0.1176 ± 0.0029	0.1926 ± 0.0026	0.6107 ± 0.0171	0.1176 ± 0.0029	0.6107 ± 0.0171	0	0.0003 ± 0.0001	0.0003 ± 0.0001	0 deg
	10 deg	0.1274 ± 0.0030	0.1989 ± 0.0026	0.6374 ± 0.0177	0.1227 ± 0.0030	0.6170 ± 0.0170	0.0042 ± 0.0001	0.0158 ± 0.0002	0.0377 ± 0.0006	$14.83 \deg \pm 0.01 \deg$
	$\Delta_{\alpha_{\infty}}\%$	$8.31\% \pm 3.69\%$	$3.26\% \pm 1.95\%$	4.38% ± 4.11%	4.33% ± 3.59%	$1.04\% \pm 3.97\%$				
LB-VLES	0 deg 10 deg $\Delta_{a_{\infty}}\%$	0.1135 0.1219 7.42%	0.1645 0.1710 3.91%	0.6898 0.7131 3.38%	0.1135 0.1174 3.46%	0.6898 0.6868 -0.43%	0 0.0044 — —	0 0.0152 — —	0 0.0362 — —	16.08 deg

Propeller performance in the negative thrust condition (J = 1.10) at 0 deg and 10 deg angles of attack

Method	α_{∞} , deg	T_C	P_C	$\eta_{ m t}$	$T_{C_{\infty}}$	$\eta_{\mathrm{t}_{\infty}}$	Y_C	N_C	$N_{C_{\infty}}$	$\Delta\phi$ [deg]
Experiment	0 deg	$-0.1073~\pm$	$-0.0416 \pm$	$0.3877~\pm$	$-0.1073~\pm$	$0.3877~\pm$	$0.0002~\pm$	$-0.0006 \pm$	$-0.0006 \pm$	163.00 deg \pm
		0.0006	0.0003	0.0032	0.0006	0.0032	0.0001	0.0001	0.0001	0.10 deg
	10 deg	$-0.1005 \pm$	$-0.0374 \pm$	$0.3727 \pm$	$-0.1007 \pm$	$0.3715 \pm$	$0.0038 \pm$	$0.0102 \pm$	$-0.0074 \pm$	$20.55~\mathrm{deg}~\pm$
		0.0008	0.0003	0.0042	0.0008	0.0042	0.0001	0.0001	0.0002	0.01 deg
	$\Delta_{lpha_{\infty}}\%$	$-6.31\% \pm$	$-9.99\% \pm$	-3.87% \pm	$-6.09\% \pm$	-4.16% \pm				
		0.88%	0.96%	1.33%	0.87%	1.35%				
LB-VLES	0 deg	-0.0985	-0.0483	0.4908	-0.0985	0.4908	0	0	0	
	10 deg	-0.0914	-0.0433	0.4741	-0.0920	0.4712	0.0030	0.0113	-0.0047	14.99 deg
	$\Delta_{lpha_\infty}\%$	-7.18%	-10.33%	-3.39%	-6.60%	-3.99%				

relative change in performance at 10 deg AOA compared to 0 deg AOA.

A. Positive Thrust Condition (J = 0.60)

For the positive thrust condition, the simulations underpredicted thrust T_C by 3% and power P_C by 15% at 0 deg AOA compared to experiments; see Table 3. This underprediction of thrust and power in simulations leads to a 13% higher propeller efficiency η_p . Similar trends are observed at the 10 deg AOA, with underpredictions of 4 and 14% for thrust and power, respectively, resulting in a 12% overprediction of η_p . The side force Y_C from the simulation is 5% higher, while the normal force is 4% lower compared to the experiments at the 10 deg AOA. This leads to approximately 1 deg higher phase delay $\Delta \phi$ in the simulation than in the experiment. Therefore, except for the power, various performance parameters obtained from simulations reasonably agree with the experiment at both angles of attack. The underprediction of power in simulations is likely caused by the underprediction of the drag in the simulations due to the inaccurate prediction of separation bubble length and reattachment location [10,29]. Additional contributing factors may include the wall model in PowerFLOW inaccurately predicting blade skin friction as well as discrepancies between the modeled and actual shape of the rotating blade in the wind-tunnel test.

To assess the validity of the simulations for studying the impact of a nonzero AOA on propeller performance, comparing the predicted relative change in performance $\Delta_{a_{\infty}}$ at 10 deg AOA compared to the 0 deg AOA case is more informative than comparing absolute performance values. As per the experiments, increasing the AOA from 0 to 10 deg increases the thrust by $8\% \pm 4\%$, power by $3\% \pm 2\%$, and propeller efficiency by $4\% \pm 4\%$. The simulations show a similar trend with a 7% increase in thrust and a 4% increase in power, leading to a 3% increase in propeller efficiency. The experiments also show a $1\% \pm 4\%$ increase in propeller efficiency along the freestream direction $\eta_{p_{\infty}}$, while the simulations predict a small decrease. Despite the overprediction of absolute power, the simulated changes in performance with the increasing AOA lie within the experimental uncertainty, demonstrating the suitability of the simulations for studying AOA-induced effects on propeller performance when operating at positive thrust.

B. Negative Thrust Condition (J = 1.10)

Table 4 presents the simulated and measured propeller performance at 0 deg and 10 deg AOA at negative thrust (J=1.10). The experimental data show a $6\% \pm 1\%$ decrease in thrust and $10\% \pm 1\%$ decrease in power at 10 deg AOA compared to the 0 deg AOA case, leading to a $4\% \pm 1\%$ decrease in turbine efficiency η_t . The simulations capture these trends well, with a 7% decrease in thrust and a 10% decrease in power, resulting in a 3% decrease in turbine efficiency. This consistent relative change in propeller performance validates the suitability of simulations for studying AOA-induced effects on propeller performance at negative thrust conditions.

While the simulations captured the relative change in propeller performance well, differences can be observed in the absolute performance prediction compared to experiments. Specifically, the simulations underpredict thrust magnitude by 8-9% and overpredict power magnitude by 16%, resulting in a 27% higher turbine efficiency for both 0 deg and 10 deg AOA cases. At 0 deg AOA, the experimental data show a minor side force Y_C , likely due to data noise, resulting in a corresponding $\Delta \phi = 163\,$ deg, which should be considered irrelevant. At 10 deg AOA, the simulation underpredicts the side force by 21% and overpredicts the normal force by 11%, resulting in approximately 6 deg lower phase delay compared to experiments. These disparities in absolute values likely stem from limitations in modeling complex flow phenomena like separation and reattachment, as detailed in previous work by authors [29]. Consequently, the numerical simulations predict a delayed onset of separation (versus J) compared to experiments, leading to higher predicted thrust (and power) at the specified operating condition (J = 1.10). However, the performance predicted by simulations might still be representative of that obtained at a slightly lower J in the experiment.

Therefore, despite the overprediction of absolute propeller performance by simulations, the good agreement in relative changes validates their suitability for this study and for further analysis of AOA-induced effects on propeller performance.

IV. Aerodynamic Results

This section presents the aerodynamic results, which are divided into five parts. Initially, the effect of the AOA on the integrated performance is analyzed for both positive and negative thrust conditions. This is followed by an analysis of the changes in the blade loading distribution with the change in the angle of attack. The observed changes are then explained by examining the flow characteristics around the blade sections. Subsequently, a comparison of periodic and broadband fluctuations in the blade loading is presented. Finally, the propeller slipstream characteristics are analyzed.

A. Integrated Performance

This section investigates the influence of AOA on the integrated propeller performance using data obtained solely from numerical simulations (refer to Tables 3 and 4) to ensure consistency with subsequent analyses. At positive thrust, increasing the AOA from 0 deg to 10 deg increases both thrust and power magnitudes along the propeller axis by 7 and 4%, respectively. Conversely, at negative thrust, increasing AOA results in decreases in both thrust and power magnitudes along the propeller axis by 7 and 10%, respectively. These changes translate to a 3% increase in propeller efficiency η_p for the positive thrust case, whereas they translate to a 3% reduction in the turbine efficiency η_t for the negative thrust case, both calculated along the propeller axis. The observed changes in the integrated performance with the change in AOA are the result of two effects: 1) the operation of the propeller at a slightly lower freestream advance ratio due to reduced axial inflow $V_{\infty}\cos\alpha_{\infty}$ and 2) the nonlinear nature of the $T_C - J$ and $P_C - J$ curves. A detailed explanation for these trends is given when analyzing the blade loading distributions in Sec. IV.B.

The direction of normal and side forces remains unaffected by the reversal of the thrust and torque direction between positive and negative thrust cases. This results in a phase difference of about 15 deg for both positive and negative thrust cases. For the positive thrust case, the normal force perpendicular to the freestream direction $N_{C_{\infty}}$ becomes more than double the normal force perpendicular to the propeller axis N_C due to the positive contribution from thrust T_C . This translates to a positive lift force $0.30T_{C_{\infty}}$ being generated in the positive thrust case. Conversely, at negative thrust, the normal force perpendicular to the freestream direction $N_{C_{\infty}}$ becomes negative (reversed in direction) due to the opposing contribution from the thrust component [refer to Eq. (5)]. This translates to a small negative lift force $0.05T_{C_{\infty}}$ being generated in the negative thrust case.

Further, in the positive thrust case, the contribution from the normal force reduces the thrust magnitude along the freestream direction ($T_{C_{\infty}}=0.1174$) compared to that along the propeller axis ($T_{C}=0.1219$). In contrast, at negative thrust, the contribution from the normal force results in a higher thrust magnitude along the freestream direction ($|T_{C_{\infty}}|=0.0920$) than that along the propeller axis ($|T_{C}|=0.0914$). Consequently, though the propeller efficiency along the propeller axis η_{p} is higher at 10 deg AOA compared to 0 deg AOA for the positive thrust case, the propeller efficiency along the freestream direction $\eta_{p_{\infty}}$ remains nearly unaffected when changing the AOA.

Given that operating the propeller at a positive thrust and positive AOA generates a positive lift, installing the propeller at such an AOA may prove beneficial at aircraft level. However, at negative thrust, the turbine efficiency along the freestream direction η_{I_∞} is reduced by 4% at 10 deg AOA compared to 0 deg AOA. Therefore, such an installation would yield a lower harvested energy than the operation at 0 deg AOA and the generation of a negative lift when operated at negative thrust.

B. Propeller Blade Loading

This section analyzes the impact of the nonzero AOA $(\alpha_{\infty} = 10 \text{ deg})$ on the propeller blade loading compared to the baseline case ($\alpha_{\infty}=0$ deg). Figures 7a and 8a show the change in the magnitude of the phase-locked local thrust coefficient $(\Delta | \overline{T_c'}(r,\phi)| = | \overline{T_c'}(r,\phi)|_{a_\infty=10~{\rm deg}} - | \overline{T_c'}(r,\phi)|_{a_\infty=0~{\rm deg}})$ at 10 deg AOA compared to 0 deg AOA. The phase-locked averaging is performed using the data from eight rotations and all the blades, resulting in a total of 24 samples for each radial and azimuthal location. Positive values indicate increased thrust magnitude, while negative values indicate decreased thrust magnitude. The noisy fluctuations in these figures are attributed to the limited data available (eight rotations) due to computational constraints. Despite the fluctuations, the presented results provide valuable insights into the blade loading changes under nonzero angles of attack. Further, Figs. 7b and 8b show the azimuthal average of the phase-locked thrust coefficient to represent a mean blade loading $(\overline{T}_c^{mean}(r))$ $(1/2\pi)\int_0^{2\pi} \overline{T_c'}(r,\phi) d\phi$ experienced by the propeller blade at both 0 deg and 10 deg AOA. Along with this mean, the spread of phase-locked thrust distribution over the azimuth $(\overline{T_c}^{\text{spread}}(r))$ $[\min(\overline{T_c'}(r,\phi)), \max(\overline{T_c'}(r,\phi))]$) is also shown to indicate the periodic variation in the blade loading over a rotation.

1. Positive Thrust Condition (J = 0.60)

The effect of nonzero AOA on propeller blade loading is well established for the positive thrust conditions [37–39]. As shown in Fig. 7a, the decrease in the local advance ratio on the advancing side leads to an increase in thrust, while the opposite is seen on the retreating side. At positive thrust, $T_C \propto J^{-2}$ and $P_C \propto J^{-3}$. Consequently, a decrease in the advance ratio on the advancing side results in a more pronounced increase in thrust and power compared to the decrease experienced on the retreating side, due to the corresponding increase in its advance ratio. Hence, operating a propeller at nonzero AOA in positive thrust conditions always leads to a higher thrust and power along the propeller axis [37–39]. This is also evident from Fig. 7b. The mean thrust distribution at the 10 deg AOA is higher than at 0 deg AOA along the whole blade span, resulting in a 7% increase in the time-averaged integrated thrust, as reported in Table 3.

Though the maximum change in advance ratio occurs at $\phi = 90$ deg and 180 deg (Fig. 4a), the highest change in thrust distribution occurs around $\phi = 105$ deg and 285 deg (Fig. 7a). This shift in the maximum and minimum thrust distribution location is a consequence of the delay in the aerodynamic response to the sinus-oidal variation in inflow angle [36]. A similar delay in the tangential force leads to a side force, as explained previously in Sec. II.D.3.

In Fig. 7b, the maximum absolute increase in the mean blade loading is observed near the peak of the loading distribution (0.6R-0.8R). As expected, the spread of the phase-locked thrust over the azimuth is negligible at 0 deg AOA due to the almost steady solution for this operation condition. In contrast, at 10 deg AOA, the

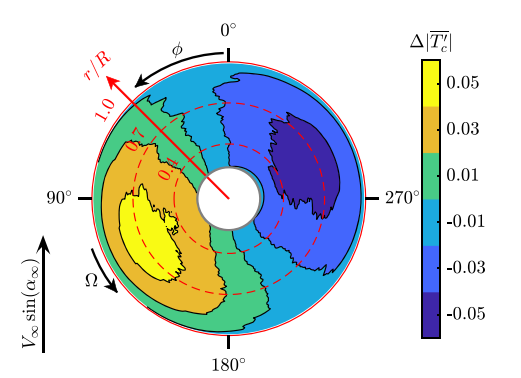
highest absolute spread occurs at the radial locations with the maximum loading at 0 deg AOA, that is, around 0.7*R*. The smallest thrust spread is seen near the propeller tip due to the combined effects of the lowest change in advance ratio and the comparatively low absolute blade loading. Notably, the region near the hub experiences a significant spread in the phase-locked thrust over the azimuth despite low absolute blade loading, primarily driven by the maximum change in advance ratio, as seen in Fig. 4a.

2. Negative Thrust Condition (J = 1.10)

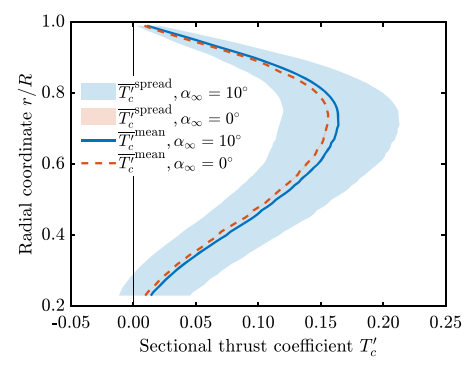
Previous studies investigating propeller operation at negative thrust [7,8,11] observed a nonmonotonic trend for the T_C-J and P_C-J curves. Up to the maximum power output point, both T_C and P_C magnitude increase with the increase in J. In other words, the gradients of the absolute value of the thrust and power coefficients with advance ratio $((\partial|T_C|/\partial J),(\partial|P_C|/\partial J))$ in negative thrust conditions have an opposite sign as compared to positive thrust conditions up to the maximum power output point. Beyond this point, the T_C , and P_C magnitudes decrease with the increase in J, resembling the performance trend of positive thrust conditions, albeit with reduced gradient. Therefore, the performance change in the negative thrust condition with the change in AOA depends upon the chosen operating condition.

For the investigated propeller, the maximum power output occurs at approximately J=1.15 [8]. Because the freestream advance ratio (J=1.10) is lower than at the maximum power output point (J=1.15), the decrease in the local advance ratio on the advancing side at 10 deg AOA compared to 0 deg AOA results in a decrease in the absolute thrust values (Fig. 8a), contrary to positive thrust conditions. On the retreating side, $\partial |T_C|/\partial J$ approaches a plateau with the increase in the local advance ratio resulting in only a small increase in thrust as evident in Fig. 8a.

Figure 8b presents the mean thrust distribution along with the spread of phase-locked thrust over the azimuth. Because of the dominance of flow separation in negative thrust conditions, the spread of phase-locked thrust over the azimuth is also visible at 0 deg AOA, with a maximum spread of $\pm 3\%$ occurring at the radial location with the peak blade loading (0.85R). This spread is a consequence of the flow separation around the blades, resulting in unsteady flow behavior in the negative thrust condition even at 0 deg AOA. Compared to the 0 deg AOA case, the 10 deg AOA case exhibits a lower absolute mean blade loading across the entire blade span, resulting in a 7% lower integrated thrust as reported in Table 4. Interestingly, the maximum spread of phase-locked thrust at 10 deg AOA occurs near the hub region, contrasting with the positive thrust condition where the maximum spread was observed around the radial location of peak loading. This different behavior is attributed to the dynamic stall of the blade sections near the hub (discussed in Sec. IV.C) and completely separated blade sections outboard, leading to a more pronounced spread of phase-locked thrust over the azimuth near the hub and the smallest spread at the blade tip.

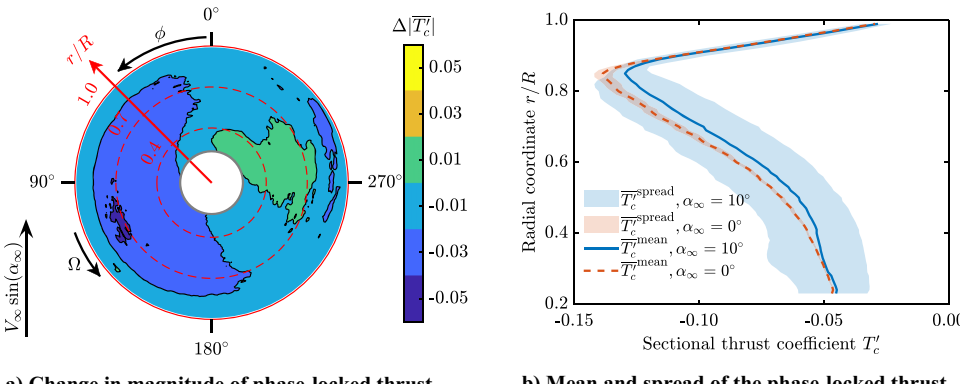


a) Change in magnitude of phase-locked thrust distribution per blade over the azimuth



b) Mean and spread of the phase-locked thrust distribution per blade

Fig. 7 Phase-locked thrust distribution per blade at nonzero angle of attack (10 deg) compared to 0 deg angle of attack at the positive thrust condition (J = 0.60).



a) Change in magnitude of phase-locked thrust distribution per blade over the azimuth

b) Mean and spread of the phase-locked thrust distribution per blade

Fig. 8 Phase-locked thrust distribution per blade at nonzero angle of attack (10 deg) compared to 0 deg angle of attack at the negative thrust condition (J = 1.10).

C. Flow Around Blade Sections

This section analyzes the influence of the varying in-plane velocity component over the azimuth on the aerodynamics of blade sections at two radial locations: near the root (r/R=0.30) and the region of maximum loading (r/R=0.70). For this purpose, chordwise pressure distributions have been analyzed for both positive and negative thrust conditions. The change in chordwise pressure distributions is explained with the help of variation of the geometric angle of attack over the azimuth. In addition, the streamlines and local static pressure contours are also shown around these blade sections at different azimuth positions.

1. Positive Thrust Condition (J = 0.60)

Figure 9a shows the change in the local geometric angle of attack at $\alpha_{\infty} = 10$ deg compared to $\alpha_{\infty} = 0$ deg $(\Delta \alpha_{g_x} =$

 $\alpha_{g_{r_{a_{\infty}}=10~{\rm deg}}}-\alpha_{g_{r_{a_{\infty}}=0~{\rm deg}}})$ for the positive thrust condition. The geometric AOA is changed slightly (<0.5 deg) at $\phi=0$ deg and 180 deg for $\alpha_{\infty}=10$ deg compared to $\alpha_{\infty}=0$ deg due to the reduced axial inflow $V_{\infty}\cos\alpha_{\infty}$. As expected, the maximum change in geometric angle occurs at $\phi=90$ deg and 270 deg with the inboard section (r/R=0.30) experiencing a higher change than the outboard section (r/R=0.70).

Figures 9b and 9c show the variation in the chordwise static pressure distributions during the rotation, and Fig. 10 shows the streamlines around the blade sections over the azimuth at r/R = 0.30 and 0.70 for the positive thrust condition, respectively. It should be noted that the y axis of the chordwise pressure distributions has been reversed to keep the front side of the propeller on top (same as Fig. 10). A direct impact of the variations in geometric angles of attack can be seen on the chordwise pressure distributions in Figs. 9b

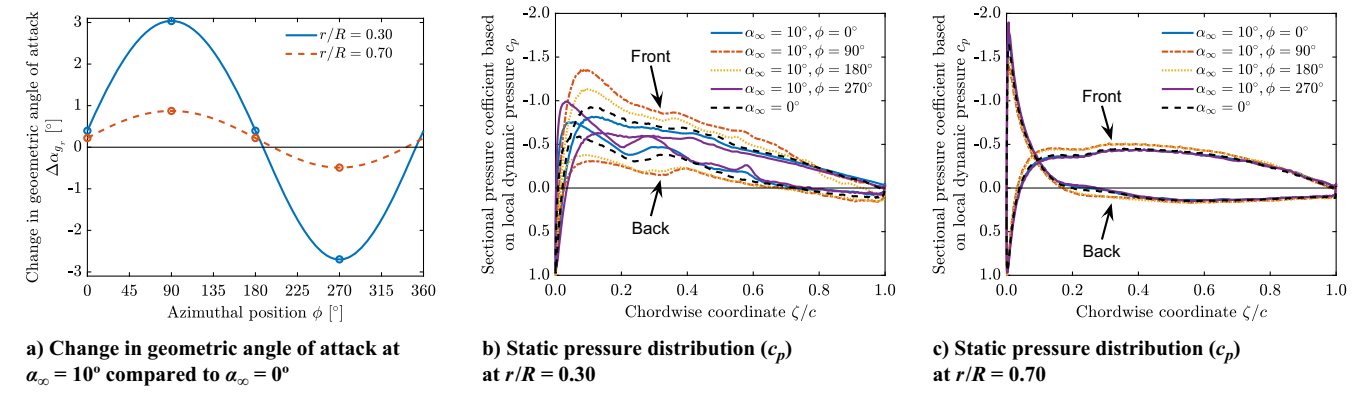


Fig. 9 Influence of α_{∞} on the local geometric angle of attack ∞_{g_e} and chordwise static pressure distribution c_p for the positive thrust condition (J=0.60).

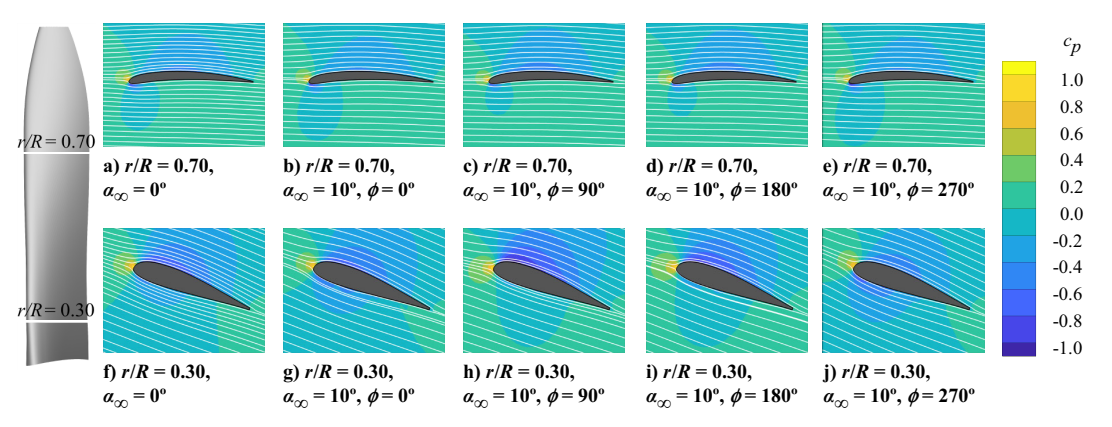


Fig. 10 Phase-locked, time-averaged streamlines around blade sections along with c_p contours at different radial locations r/R for the positive thrust condition (J=0.60).

and 10g-10j for r/R=0.30. As the highest angle of attack is expected at $\phi=90$ deg for $\alpha_{\infty}=10$ deg case, the highest pressure difference between the front and back sides of the blade section is also observed at $\phi=90$ deg. As the angle of attack decreases from $\phi=90$ deg to $\phi=270$ deg, the pressure difference between the front and back sides also decreases. Though the geometrical angle of attack is the same at $\phi=0$ deg and $\phi=180$ deg, the former shows a lower pressure difference between the front and back sides of the blade section compared to the latter due to the aerodynamic delay in response to the sinusoidal variation in the geometric angle of attack. As a result of this aerodynamic delay, though the $\phi=0$ deg for $\alpha_{\infty}=10$ deg case has a higher geometrical angle of attack than $\alpha_{\infty}=0$ deg case, the pressure difference between the front and back sides is lower for the former.

At r/R=0.70, the geometric AOA changes by only 1 deg and -0.5 deg at $\phi=90$ deg and 270 deg, respectively, with respect to $\alpha_{\infty}=0$ deg; see Fig. 9a. The change is comparatively small in the local static pressure coefficient between different azimuthal positions; see Figs. 9c and 10b–10e. The highest pressure difference between the front and back sides of the blade section is seen at $\phi=90$ deg due to the highest geometric angle of attack, and the lowest pressure difference between the front and back sides is seen at $\phi=270$ deg due to the lowest geometric angle of attack. This shows that the dominant effect is the variation in the local dynamic pressure at this blade section, leading to a significant change in the local thrust coefficient over the azimuth (Fig. 7a), and is only marginally affected directly by the blade section performance.

2. Negative Thrust Condition (J = 1.10)

At J=1.10, the crossflow component results in a larger change in the geometric AOA compared to the J=0.60 case. Specifically, at r/R=0.30, there is a ± 6 deg change in geometric AOA at $\phi=90$ deg and 270 deg, respectively, whereas at r/R=0.70, the

respective change is 3 deg and -2 deg; see Fig. 11a. The highest positive change in the angle of attack at $\phi = 90$ deg results in an absolute lower angle of attack at the blade section, resulting in the smallest separation bubble at the blade sections for both r/R = 0.30and 0.70 in Figs. 11b and 11c. Streamline visualizations in Figs. 12c and 12h further support this observation. As the angle of attack becomes more negative from $\phi = 90$ deg to $\phi = 270$ deg, the size of the separation bubble increases for both radial locations (Fig. 12). Though $\phi = 0$ deg and $\phi = 180$ deg have the same geometric angle of attack, the separation bubble is larger at $\phi = 0$ deg compared to $\phi = 180$ deg; see Figs. 11b and 11c. This is a consequence of the delay in the aerodynamic response to the sinusoidal variation in the geometric angle of attack. These sinusoidal variations in the geometric angle of attack experienced by the blade sections are analogous to a plunging airfoil, leading to dynamic stall conditions at the negative thrust condition.

D. Broadband Fluctuations

When propeller blades operate in negative thrust conditions, the flow separation around them causes broadband fluctuations in blade loading, which act as sources of both noise and structural vibrations [10]. To obtain the broadband fluctuations over the azimuth, the phase-locked local thrust coefficient $\overline{T_c'}(r,\phi)$ was subtracted from the instantaneous local thrust coefficient $T_c'(r,\phi,t_{\rm sim})$. Figure 13 displays the rms of the resulting broadband fluctuations of local thrust coefficient $\sigma(T_c'(r,\phi))$ over eight rotations, normalized with the absolute mean thrust distribution $|\overline{T_c'}^{\rm mean}(r)|$, for both the positive and negative thrust conditions.

At 0 deg AOA, the positive thrust condition (J = 0.60) has negligible broadband fluctuations as evident from Fig. 13a. In contrast, significant fluctuations can be observed at the negative thrust condition (J = 1.10) in Fig. 13b. The fluctuations increase in the negative thrust condition with radial location due to the increasing

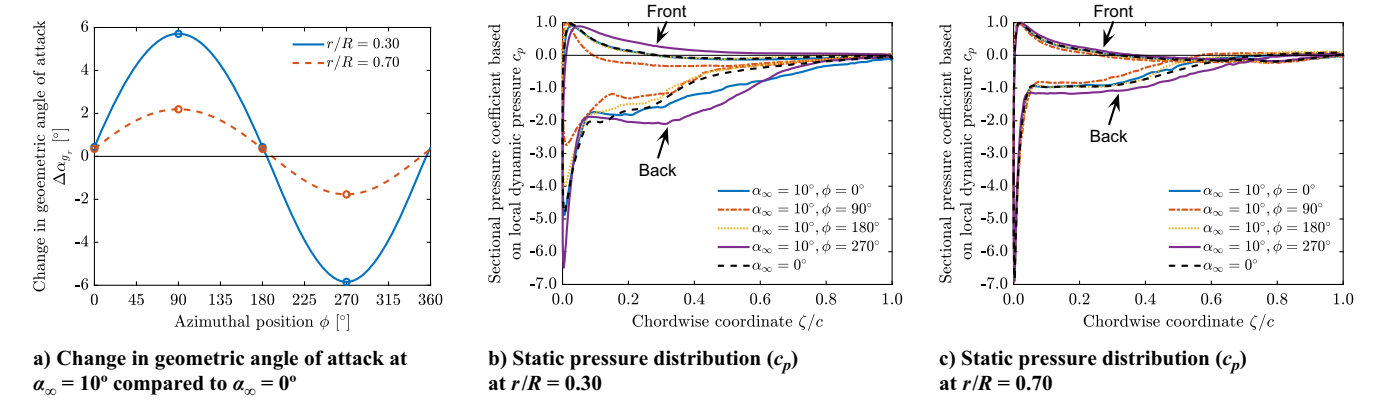


Fig. 11 Influence of α_{∞} on the local geometric angle of attack (α_{g_r}) and chordwise static pressure distribution (c_p) for the negative thrust condition (J=1.10).

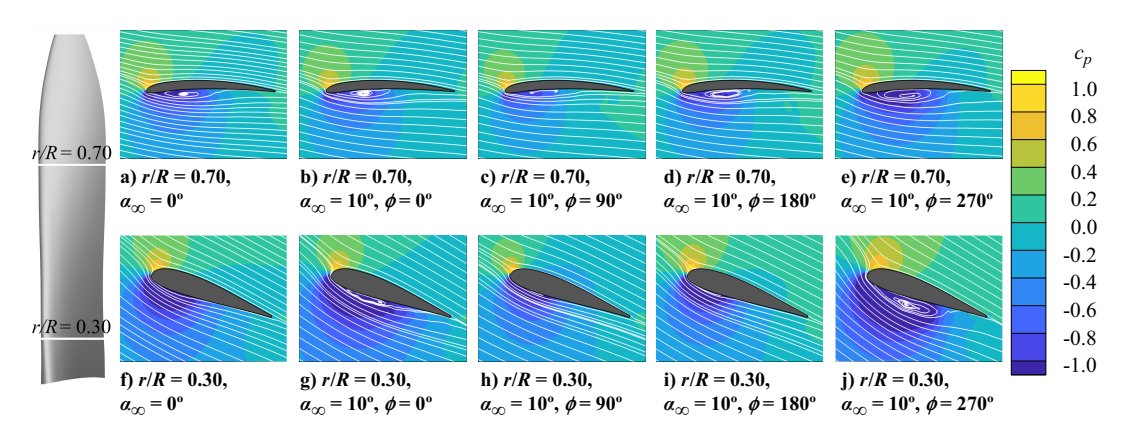


Fig. 12 Phase-locked, time-averaged streamlines around blade sections along with c_p contours at different radial locations r/R for the negative thrust condition (J=1.10).

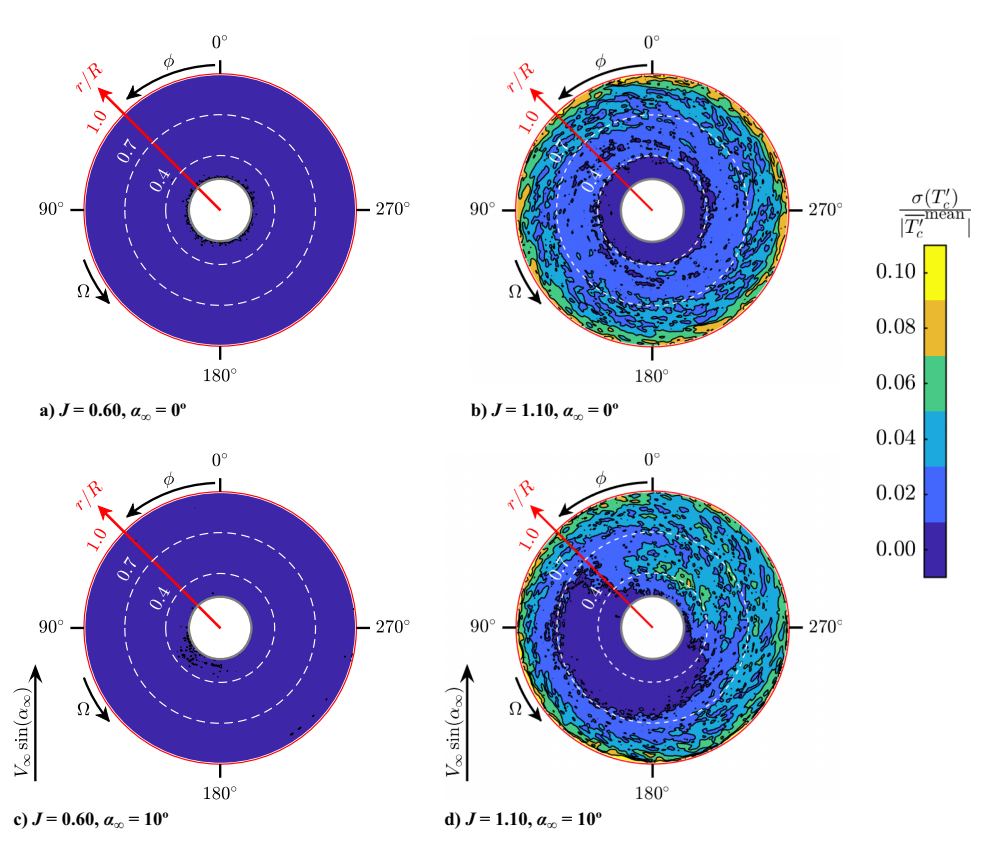


Fig. 13 Normalized broadband fluctuations in phase-locked thrust distribution at 0 deg and 10 deg angle of attack at the positive (J = 0.60) and negative (J = 1.10) thrust conditions.

separation as observed in previous work [7,10]. For the inboard part of the blade, where the flow is attached, the fluctuations are nearly negligible up to r/R = 0.40. However, in the midboard sections (0.40 < r/R < 0.70), the fluctuations are around 2–3% of the mean thrust level and increase up to 10% or even more at the blade tip.

The 10 deg AOA case also shows negligible broadband fluctuations in the positive thrust condition; see Fig. 13c. In contrast, the operation of the propeller at 10 deg in the negative thrust condition changes the distribution of broadband fluctuations over the blade as compared to 0 deg AOA; see Figs. 13b and 13d. As the inboard part of the blade exhibits dynamic stall (Fig. 12), during the part of the rotation ($\phi = 75$ –195 deg) over which the flow is almost fully attached, fluctuations with negligible amplitude are observed for $r/R \le 0.70$. However, as the separation bubble extends to the trailing edge on the retreating side, it leads to fluctuations of around 5% of the mean thrust level. Even on the outer part of the blade, the fluctuations are amplified on the retreating side and are comparatively reduced on the advancing side, as expected.

1. Relative Amplitudes of Periodic and Broadband Fluctuations

Given the increased broadband fluctuations in the negative thrust condition, a quantitative analysis of the relative amplitudes of periodic and broadband fluctuations is necessary. For this purpose, the absolute mean thrust value $|\overline{T_c^{\prime}}^{\text{mean}}(r)|$, previously shown in Figs. 7b and 8b, has been subtracted from the phase-locked thrust coefficient $\overline{T_c^{\prime}}(r,\phi)$. The resulting quantity has been normalized with the absolute mean thrust value $|\overline{T_c^{\prime}}^{\text{mean}}(r)|$ to asses the periodic variation in the local thrust coefficient. The amplitude of broadband fluctuations has been indicated with the shaded regions showing the standard deviation of the quantity.

Figure 14 displays the periodic variations along with broadband fluctuations of the local thrust coefficient at three radial stations: r/R = 0.30, 0.70, and 0.90, which correspond to the near blade root, maximum-loading region, and near blade tip, respectively. There is almost 180 deg phase difference between positive and negative thrust conditions due to the opposite change in the absolute thrust on the advancing and retreating side as seen previously in Figs. 7a and 8a.

At r/R = 0.30 in Fig. 14a, the positive thrust condition displays a larger range of periodic variations in the local thrust coefficient (-94 to 109%) compared to the negative thrust condition (-33 to 41%). This contrasts with the larger variations in the local advance ratio observed in the negative thrust condition in Fig. 4. It can be attributed to two factors. First, the given blade section has a lower

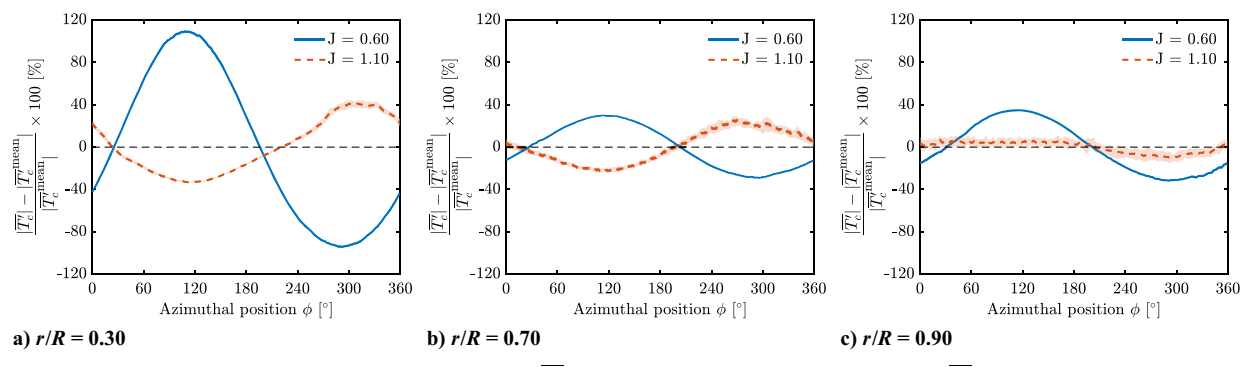


Fig. 14 Change in the absolute phase-locked thrust coefficient $|\overline{T'_c}|$ with respect to the absolute mean value $|\overline{T'_c}|^{\text{mean}}|$ over the azimuthal position ϕ .

mean loading in the positive thrust condition ($|\overline{T_c'}^{\text{mean}}| = 0.034$) than the negative thrust condition ($|\overline{T_c'}^{\text{mean}}| = 0.049$), as shown in Figs. 7b and 8b. This results in a higher relative periodic variation in the positive thrust condition even for similar absolute changes in the thrust coefficient. Second, the thrust coefficient has reduced sensitivity to the changes in the advance ratio at negative thrust conditions, as depicted in the $T_C - J$ curve in previous studies [7,8,11]. Specifically, the blade section operates at high negative angles of attack, which leads to the formation of a leading-edge separation bubble that reduces the $C_l - \alpha$ slope, consequently reducing the sensitivity of the thrust coefficient to advance ratio variations. The positive thrust condition exhibits broadband fluctuations amplitude up to $\pm 2\%$ of the mean thrust value, whereas the negative thrust condition shows broadband fluctuations of up to $\pm 4\%$ of the mean thrust value. The higher broadband fluctuations in the negative thrust condition are caused by the observed separation bubble at this radial location in Fig. 12.

At r/R=0.70, the relative maximum amplitude of the periodic variation in thrust coefficient is reduced to 30 and 25% of the mean thrust value for the positive and negative thrust conditions, respectively. The broadband fluctuations are negligible in the positive thrust condition, with variations of up to $\pm 1\%$ of the mean thrust value. In contrast, they are noticeable in the negative thrust condition, reaching up to $\pm 7\%$ of the mean thrust value between 180 deg $\leq \phi \leq$ 360 deg. The increased broadband fluctuations on the retreating side are attributed to the periodic appearance of the separation bubble, as seen in Fig. 12.

At r/R = 0.90, the positive thrust condition shows the relative amplitude of periodic variations of up to 35% of the mean thrust value with negligible amplitude of broadband fluctuations (up to $\pm 2\%$ of the mean thrust value). Interestingly, the negative thrust condition no longer displays a sinusoidal pattern observed at inboard sections (Fig. 14c). The periodic fluctuations become nonsinusoidal and exhibit a reversal in trend compared to the inboard sections. This is expected to be the consequence of the operation of the blade section in the deep stall region, where the increase of the absolute AOA on the retreating side (180 deg $\leq \phi \leq$ 360 deg) leads to a decreased C_l and

the corresponding lower thrust coefficient. At this radial station, the broadband fluctuations (up to $\pm 7\%$ of the mean thrust value) appear to be almost as significant as the periodic fluctuations, which range from -10 to 7% of the mean thrust value.

E. Propeller Slipstream

In a tractor propeller—wing configuration, the interaction between the propeller slipstream and wing significantly affects the wing performance. These changes are mainly determined by two parameters: the swirl angle induced by the propeller slipstream and the modification of the dynamic pressure. Therefore, this section presents an analysis of these two parameters for the positive and negative thrust conditions, both at zero and nonzero angles of attack. All the results presented in this section are obtained at x/R=1.0 on a plane parallel to the propeller plane. This axial position has been based on the potential location of a lifting surface (wing). The projected propeller disk is shown in the figures with the help of a dashed-red line indicating r/R=1.0.

1. Swirl Angle

Figure 15 shows the time-averaged swirl angle θ_{swirl} calculated using Eq. (7). The swirl angle has been defined as positive in the direction of propeller rotation. It is important to highlight that the inplane freestream velocity component has been subtracted from the tangential velocity to isolate and account for the swirl induced solely by the propeller,

$$\theta_{\text{swirl}} = \tan^{-1} \left(\frac{V_{\text{t}} - V_{\infty} \sin(\alpha_{\infty}) \sin(\phi)}{V_{\text{a}}} \right) \tag{7}$$

At $\alpha_{\infty} = 0$ deg, as expected, there is an axisymmetric swirl in the propeller slipstream; see Figs. 15a and 15b. The operation at the positive thrust condition (J = 0.60) introduces a positive swirl of about +3 deg to +4 deg (Fig. 15a), with contraction of the slipstream to 0.93R at x/R = 1.0 (indicated by the outer edge of the positive swirl contour). On the other hand, in the negative thrust

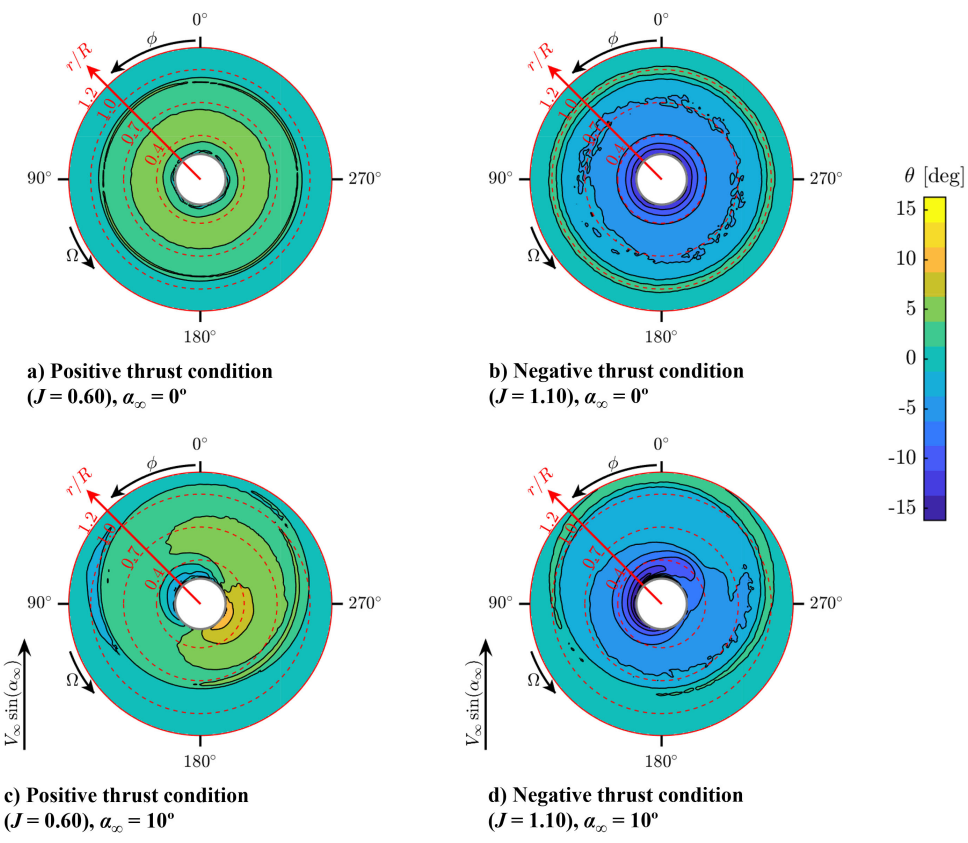


Fig. 15 Time-averaged swirl angle θ_{swirl} in the propeller slipstream at x/R = 1.0.

condition (J=1.10), the propeller introduces a negative swirl in the slipstream with strong radial gradients. Near the hub, the swirl angle is about -12 deg, reducing to -5 deg at 0.5R and -4 deg to -2 deg in the outboard region (Fig. 15b). This steep radial gradient of swirl angle in the inboard sections results from high inboard torque loading in the negative thrust conditions [10]. Additionally, the stall of the propeller tip leads to positive torque loading on the blade tip, resulting in a positive swirl (+2 deg) near the edge of the slipstream.

At the 10 deg angle of attack, the slipstream is deflected outside the projected propeller region (r/R>1.0) above the nacelle and distorted beneath it due to the in-plane velocity component of the freestream $(V_{\infty}\sin\alpha_{\infty})$; see Figs. 15c and 15d. In the inboard region, the root vortices induce a negative swirl, whereas the potential flowfield induced by the nacelle (due to the in-plane velocity component) generates a negative swirl on the advancing side and a positive swirl on the retreating side. The combined effect of the two (root vortex and potential flowfield induced by nacelle) results in a negative swirl on the advancing side for both positive and negative thrust conditions Figs. 15c and 15d. Conversely, on the retreating side, these effects partially cancel out, leading to a positive swirl for the positive thrust condition and a small negative swirl for the negative thrust condition.

Away from the nacelle $(r/R \ge 0.7)$, the increased tangential velocity on the advancing side relative to the 0 deg AOA case is balanced by the corresponding increase in axial velocity, while the decreased tangential velocity on the retreating side is balanced by the decrease in axial velocity. This results in similar swirl values as in the case of 0 deg AOA for both positive and negative thrust conditions. For the negative thrust condition, as the stall of the blade tip is more pronounced on the retreating side (shown previously in Fig. 12), a positive torque is required to propel the tip along with the blade, resulting in a slight positive swirl around r/R = 1 on the retreating side as shown in Fig. 15d.

Additionally, in Fig. 15c, the slipstream appears slightly shifted toward the retreating side in the positive thrust condition due to a

more significant contraction on the advancing side than on the retreating side. Conversely, the retreating side experiences more expansion in the negative thrust condition, leading to a similar apparent shift in Fig. 15d.

2. Dynamic Pressure

Figure 16 shows the squared magnitude of the normalized velocity within the propeller slipstream. This quantity directly reflects changes in dynamic pressure compared to the freestream condition. At the 0 deg angle of attack, the dynamic pressure distribution in the slipstream exhibits axisymmetric behavior for both positive and negative thrust conditions. Operation under positive thrust conditions (Fig. 16a) results in increased dynamic pressure in the slipstream compared to the freestream, reaching approximately 30% around 0.4R and 40% between 0.5R and 0.8R for the selected thrust setting ($T_C = 0.11$); see Fig. 16a. On the other hand, the operation at negative thrust (Fig. 16b) results in a decrease in dynamic pressure within the slipstream compared to the freestream. This decrease is approximately 20% between 0.3R and 0.7R and 30% between 0.7R and 0.9R for the selected thrust setting ($T_C = -0.10$); see Fig. 16b.

Upon increasing the angle of attack from 0 deg to 10 deg, the dynamic pressure distribution within the propeller slipstream is no longer axisymmetric (as expected). In the positive thrust condition (Fig. 16c), the advancing side experiences a dynamic pressure increase of up to 60% compared to the freestream, while the retreating side sees a maximum increase of 40%. Consequently, there is effectively higher dynamic pressure on the advancing side and lower dynamic pressure on the retreating side compared to the 0 deg AOA case. These variations in dynamic pressure are directly related to the changes in the blade loading distribution shown in Fig. 7a. In the inboard regions, the presence of the nacelle disrupts the in-plane velocity component of the freestream, resulting in a region of reduced dynamic pressure (deficit) above it, as observed in Fig. 16c. This region of the deficit is further amplified by the negative blade loading in the inboard part of the blade on the

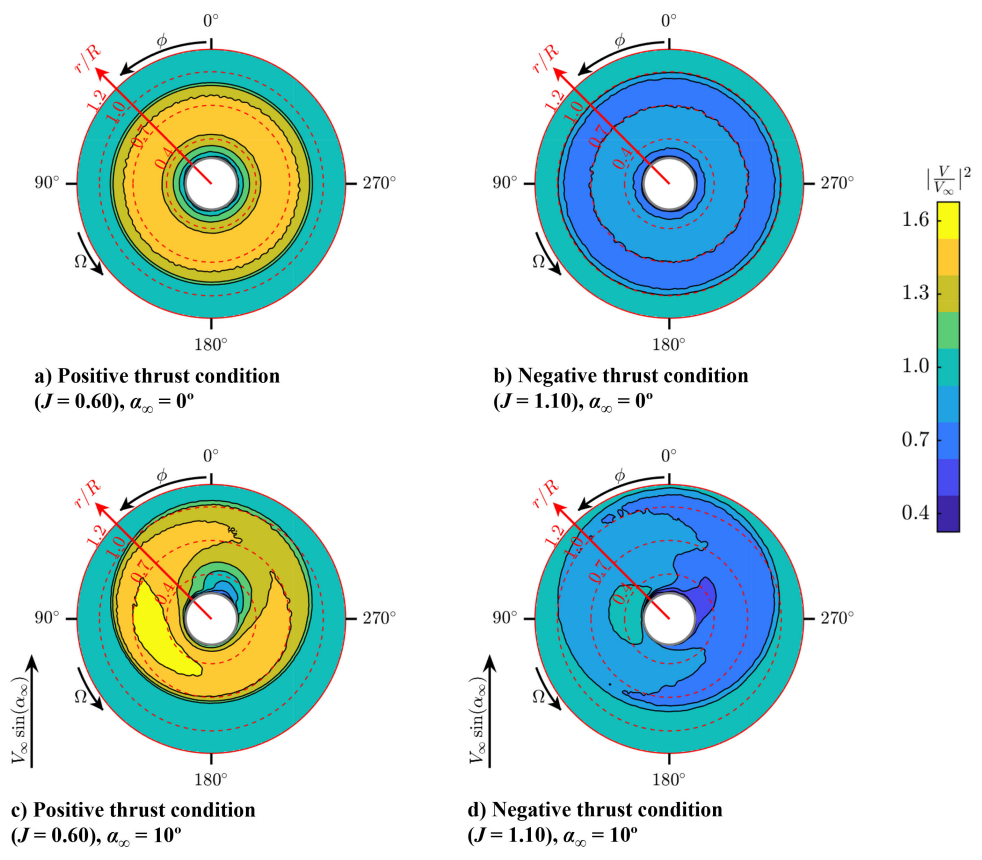


Fig. 16 Time-averaged dynamic pressure $(|V/V_{\infty}|^2)$ in the propeller slipstream at x/R = 1.0.

retreating side, as indicated by the lower bound of the $\overline{T_c'}^{\text{spread}}$ in Fig. 7b.

For the negative thrust condition (Fig. 16d), the advancing side experiences up to 20% lower dynamic pressure compared to the freestream for $r/R \ge 0.60$, while the retreating side experiences a decrease of up to 30%. Again, this results in a higher dynamic pressure on the advancing side and lower dynamic pressure on the retreating side as compared to the 0 deg AOA case. These changes in the dynamic pressure correspond directly to the observed changes in the blade loading in Fig. 8. For r/R < 0.60, the combined effects of the tangential velocity induced by the propeller and the velocity induced by the nacelle's potential flowfield result in up to 5% decrease in dynamic pressure on the advancing side and up to 40% decrease on the retreating side.

3. Inferences for Potential Wing Immersed in Propeller Slipstream

Based on the results shown in Figs. 15 and 16, it is evident that a wing immersed in a slipstream experiences distinct effects depending on the thrust condition and angle of attack. This section focuses on the effects of the propeller slipstream on the wing, without addressing the influence of the wing on propeller performance. It assumes that the propeller and wing have the same sign of AOA (both positive or both negative).

At a negative thrust condition at 0 deg AOA, the slipstream induces a negative swirl and a reduced dynamic pressure compared to the slipstream at a positive thrust condition. The negative swirl increases the effective AOA on the advancing side, while decreasing it on the retreating side. Therefore, the part of the wing located on the retreating side experiences a double negative effect: decreased dynamic pressure and a decreased angle of attack due to the swirl. In contrast, on the advancing side, the effect of the decreased dynamic pressure is partially compensated by the increased angle of attack induced by the swirl. Therefore, the impingement of the slipstream of a propeller operating at negative thrust conditions results in a higher reduction in the lift on the retreating side than on the advancing side.

Operation of a propeller at negative thrust conditions at a nonzero angle of attack results in a higher dynamic pressure on the advancing side and a lower dynamic pressure on the retreating side compared to the 0 deg AOA. Assuming the propeller and wing have the same sign of AOA, the higher dynamic pressure, coupled with the beneficial impact of the negative swirl on the angle of attack, enhances lift generation on the advancing side compared to 0 deg AOA. Conversely, on the retreating side, the lower dynamic pressure and the adverse effect of the negative swirl on the angle of attack result in a lower lift generation than at 0 deg AOA. Therefore, when the propeller and wing have the same sign of AOA, a nonzero AOA further amplifies the differences in the lift generated on the advancing and retreating sides at negative thrust conditions.

In the positive thrust condition, the positive swirl induced by the slipstream reduces the effective angle of attack on the advancing side and increases the effective angle of attack on the retreating side. On the advancing side, the decrease in the effective angle of attack due to the swirl is partially countered by the increase in the dynamic pressure. Conversely, on the retreating side, both the increased dynamic pressure and the increased effective angle of attack due to the swirl angle result in an increase in lift. At a nonzero AOA, the part of the wing on the advancing side experiences a higher dynamic pressure and lower positive swirl, leading to a higher lift compared to the 0 deg AOA scenario. Conversely, on the retreating side, the decrease in dynamic pressure results in a lower lift generation than the 0 deg AOA case. Therefore, in contrast to the negative thrust conditions, when the propeller and wing have the same sign of AOA, a nonzero AOA tends to reduce the differences in the lift generated on the advancing and retreating sides at positive thrust conditions.

V. Far-Field Aeroacoustic Results

The operation of a propeller at nonzero angles of attack significantly changes the noise characteristics compared to its operation at 0 deg angle of attack [40,41]. Two mechanisms account for these changes: the periodic variations in blade loading and the asymmetric phase modulation of the strength of noise sources. The asymmetric phase modulation is the kinematic/acoustic effect, which is a result of the periodic variation of observer–source relative Mach number for an observer rigidly rotating with the blade [40,42,43]. The present study investigates the relative importance of these two effects by conducting FWH computations with and without the convective effects due to the freestream cross-flow velocity component ($V_{\infty} \sin \alpha_{\infty}$) when the propeller operates at the 10 deg angle of attack.

The far-field noise was computed on a circular array with a radius of 10D, centered around the propeller center. The array included 24 evenly spaced virtual microphones in two planes: the plane of propeller rotation (Y-Z) plane) and the plane along the axis of the propeller (X-Z) plane). To isolate the impact of the angle of attack on the noise generation mechanisms, the microphones were fixed relative to the propeller itself, meaning the microphones were kept in the same location even when the freestream was tilted to change the angle of attack.

In both planes, the total noise at the circular arrays was further decomposed into thickness and loading noise using the monopole and dipole terms, respectively, in the so-called solid FWH formulation [13,27]. The noise directivity was plotted in terms of overall sound pressure level (OSPL) in two different frequency ranges: $0.9 \leq BPF \leq 10$ and $0.9 \leq BPF \leq 1.1$, where BPF refers to blade passing frequency. The former represents the overall sound pressure level directivity, whereas the latter is used to investigate the directivity of tonal noise at the most dominant harmonic, that is, the first BPF.

Here, the lower bound of 0.9 BPF eliminates potential contributions from numerical noise sources arising due to differences in blade loading on the propeller blades. These variations are inherent to the limitations of LB–VLES working with Cartesian meshes, leading to up to $\pm 4\%$ difference in blade loadings for J=0.60 and $\pm 1\%$ difference in blade loadings for J=1.10 compared to the blade-averaged loading. The upper bound for the OSPL was set at 10 BPF, even though the simulations were configured with spatial and temporal resolutions suitable for up to 50 BPF. This choice was made because the power spectrum density (PSD) plots showed no observable difference in the broadband noise signature for BPF > 10 with changes in the angle of attack, which is in agreement with the previous investigation conducted by Romani et al. [41].

A. Noise Directivity in Plane of Propeller Rotation

1. Positive Thrust Condition (J = 0.60)

Figure 17 shows the far-field noise directivity in the plane of propeller rotation at the positive thrust condition (J=0.60). Figures 17a and 17b display the noise directivity at 0 deg and 10 deg angles of attack, respectively, for the frequency range of $0.9 \le \mathrm{BPF} \le 10$. Similarly, Figs. 17c and 17d show the noise directivity for the frequency range of $0.9 \le \mathrm{BPF} \le 1.1$. In Figs. 17b and 17d, an additional noise directivity denoted as "Total (no cross-flow)" is shown with blue-cross markers. It has been calculated without accounting for the convection effects of the freestream crossflow velocity component $V_\infty \sin \alpha_\infty$ and is used to illustrate the relevance of the aforementioned asymmetric phase modulation for the given operating condition. The corresponding power spectrum density plots are presented in Fig. 18 for $\phi=0$ deg and 180 deg.

The noise directivity at 0 deg angle of attack shows expected axisymmetry around the propeller axis; see Figs. 17a and 17c. However, when the angle of attack is changed from 0 deg to 10 deg, the noise is no longer axisymmetric around the propeller axis (Figs. 17b and 17d). The total noise increases in the region from which the propeller is tilted away, that is, 90 deg $<\phi<270$ deg, and decreases in the opposite region, that is, 270 deg $<\phi<90$ deg. These changes are in agreement with the literature [40,44–46]. The change in the noise directivity is caused by unsteady (periodic) loading on the propeller blades. The total noise calculated without accounting for the convection effects of the freestream cross-flow velocity component

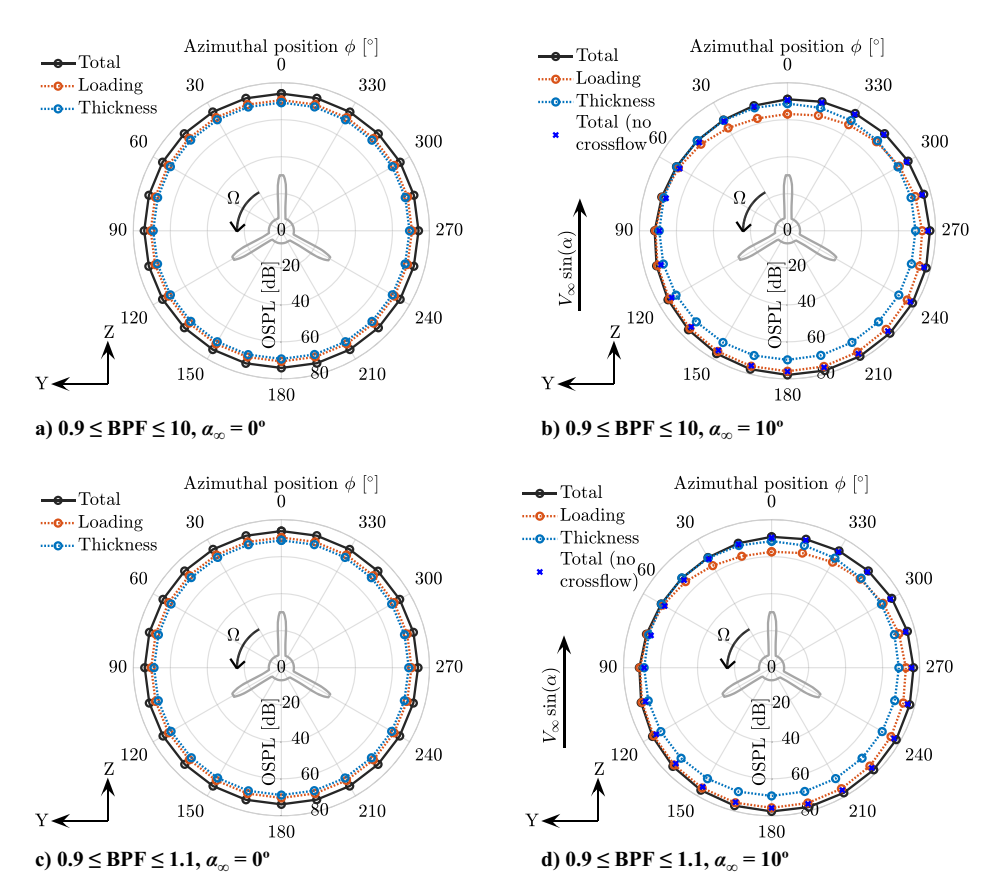


Fig. 17 Effect of angle of attack on the azimuthal noise directivity in the plane of propeller rotation at the positive thrust condition (J = 0.60).

(blue-cross markers) shows results similar to those obtained when including these convection effects. Therefore, the influence of asymmetric acoustic modulation by the crossflow velocity component is minor compared to the impact of unsteady blade loading for the given case.

The change in the angle of attack from 0 deg to 10 deg results in a maximum increment of 5 dB in noise emissions occurring at $\phi = 195$ deg and a maximum reduction of 8 dB occurring at $\phi = 15$ deg in the loading noise. This increase and decrease are direct results of the change in the blade loading at 10 deg angle of attack compared to 0 deg (Fig. 7). Because the loading noise generated by the propeller blades primarily radiates in the perpendicular direction, the maximum and minimum noise locations are located 90 deg ahead of the maximum and minimum blade loading locations, respectively.

In contrast to the loading noise, the thickness noise exhibits a negligible change $(\pm 0.5 \text{ dB})$ with the varying angle of attack. This can be attributed to the relatively smaller variation in the effective velocity at the outboard sections $(\pm 3\%$ at the blade tip) compared to

the corresponding variation in the blade loading, as previously shown in Fig. 14. At 0 deg angle of attack, the thickness noise is almost as significant as the loading noise. However, at the 10 deg angle of attack, the thickness noise becomes dominant between 300 deg < $\phi < 60$ deg due to the decrease in the loading noise, whereas the loading noise remains dominant for the rest of the azimuth.

For further insights into the spectral content of the propeller noise emissions, the PSD of the pressure signal obtained at virtual microphones is shown in Fig. 18. The PSD is presented for two azimuthal positions, 0 and 180 deg, which correspond to the regions of maximum decrease and increase of the loading noise, respectively. At 10 deg angle of attack, a decrease is observed in the first BPF at $\phi = 0$ deg and an increase at $\phi = 180$ deg, consistent with the noise directivity plots. Similar trends can be observed for the second BPF.

2. Negative Thrust Condition (J = 1.10)

The noise directivity plots for the negative thrust condition (J = 1.10) are shown in Fig. 19. An axisymmetric trend is observed

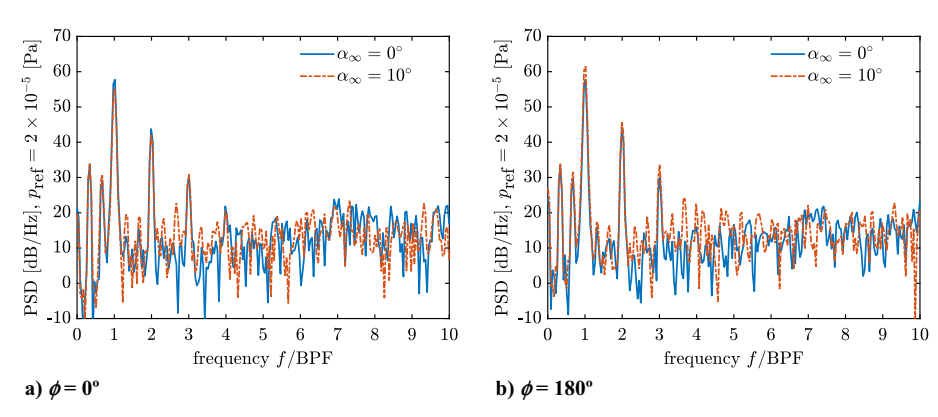


Fig. 18 Power spectrum density of the pressure signal obtained at virtual microphones located in the plane of propeller rotation at the positive thrust condition (J = 0.60).

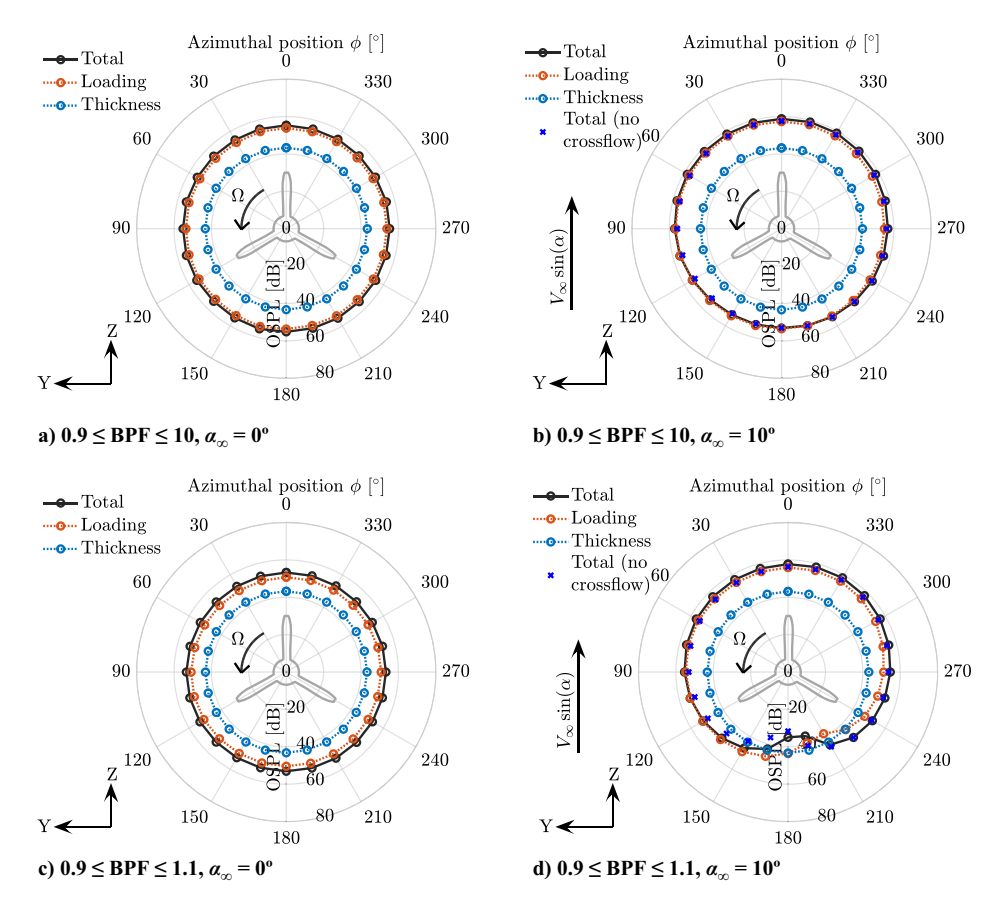


Fig. 19 Effect of angle of attack on the azimuthal noise directivity in the plane of propeller rotation at the negative thrust condition (J = 1.10).

at 0 deg angle of attack, as expected. Unlike the positive thrust case (J=0.60), the thickness noise is no longer the dominant noise source. This is because the reduced tip Mach number at J=1.10 compared to J=0.60 decreases the thickness noise, which is more sensitive to the tip Mach number than the loading noise. Additionally, the loading noise is significantly lower in the negative thrust condition compared to the positive thrust condition. This is due to the lower magnitude of T_C (Table 3), lower tip Mach number, and the inboard shift of the power distribution [7] in the negative thrust case compared to the positive thrust case.

Similar to J = 0.60, the blue-cross markers in Figs. 19b and 19d represent the noise directivity when neglecting the convection effect of the crossflow component. These markers show results very similar to the total noise with the crossflow component (Fig. 19b), indicating that the unsteady blade loading again dominates the change in the noise directivity. At 10 deg angle of attack, the total noise increases by up to 4 dB between 270 deg $\leq \phi \leq$ 90 deg and decreases by up to 2 dB between 90 deg $\leq \phi \leq$ 270 deg compared to 0 deg; see Fig. 19b. Similar changes can also be observed in the noise directivity at the first BPF in Fig. 19d. The change in angle of attack from 0 to 10 deg results in a decrease of up to 12 dB in the loading noise in the region from which the propeller is tilted away (90 deg $\leq \phi \leq$ 270 deg) and an increment of up to 6 dB in the opposite direction (270 deg $\leq \phi \leq$ 90 deg) as shown in Fig. 19c. This trend differs from the positive thrust condition (Fig. 17b), where a decrease was observed between 270 deg $\leq \phi \leq$ 90 deg and an increase was observed between 90 deg $\leq \phi \leq$ 270 deg.

The difference in the noise directivity between the positive and negative thrust conditions can be explained by revisiting the changes in blade loading shown in Fig. 14. As the variation in the absolute blade loading in the negative thrust condition is 180 deg out of phase as compared to the positive thrust condition, the corresponding changes in the loading noise directivity are also out of phase by 180 deg. Surprisingly, for this operating condition, the interference between the thickness and the loading noise becomes destructive between 120 deg $< \phi <$ 210 deg, resulting in a decreased tonal

noise. This effect is also observable in Fig. 19b, in which the total noise level is slightly lower than the loading noise levels between the aforementioned azimuthal positions. The detailed investigation into the reasons behind the observed destructive interference is presented in Sec. V.A.3.

The relative level of tonal and broadband noise can be observed by examining the PSD at two azimuthal positions: $\phi=0$ deg and $\phi=180$ deg, as shown in Fig. 20. Figure 20a depicts an increase in the noise at the first BPF at $\alpha_{\infty}=10$ deg, consistent with the results presented in Fig. 19d. The broadband noise levels are comparable at both α_{∞} values. At $\phi=180$ deg, the noise level at the first BPF is significantly reduced. However, there is an observable increase in broadband noise between 1 and 5 BPFs, which partially compensates for the decrease of the tonal noise at the first BPF. This increase in broadband noise is a result of the stalling of the blade tip, as seen in Fig. 14c.

3. Pressure Signal Peak Amplitude and Phase Difference Between Loading and Thickness Noise Signals

The destructive interference observed between loading and thickness noise for 120 deg < ϕ < 210 deg in Fig. 19d is further investigated by band passing the loading and thickness noise pressure signal at the microphones for the first BPF (0.9 \leq BPF \leq 1.1). Figures 21a and 21b show the peak amplitude of the resulting pressure signal for both thickness and loading components for the positive (J=0.60) and negative (J=1.10) thrust conditions, respectively. Further, Fig. 21c shows the phase difference between the peak amplitudes of the resulting loading and thickness noise pressure signals.

At $\alpha_{\infty} = 0$ deg, the pressure signal peak amplitudes for both thickness and loading noise exhibit minimal variation with the azimuthal position for both thrust conditions (J = 0.60 and 1.10); see Figs. 21a and 21b. The small variations in the loading noise peak amplitude at J = 1.10 result from the extensive flow separation at this condition. The pressure signal peak amplitudes at J = 1.10 are

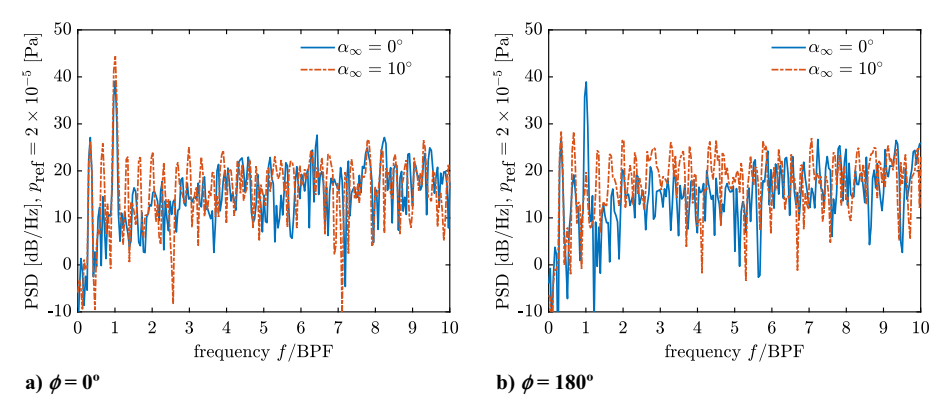


Fig. 20 Power spectrum density of the pressure signal obtained at virtual microphones located in the plane of propeller rotation at the negative thrust condition (J = 1.10).

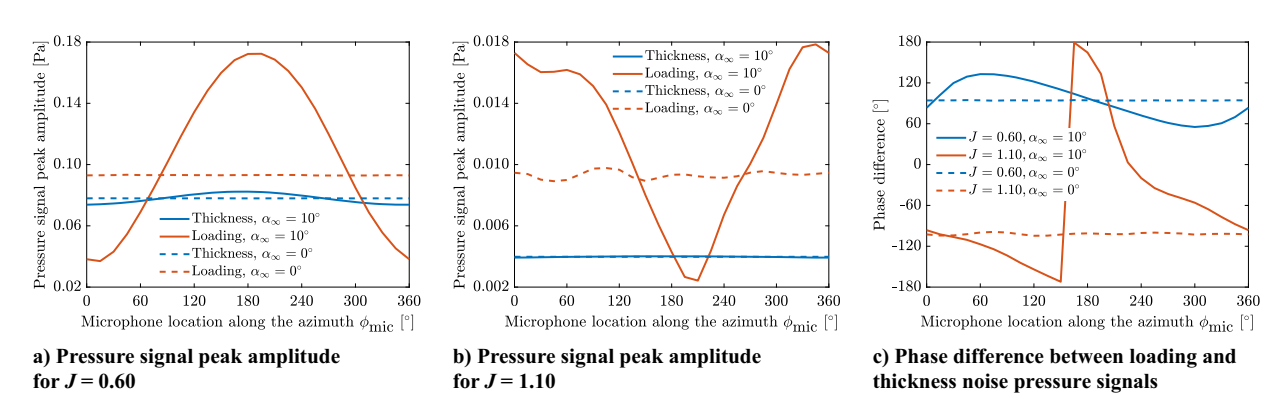


Fig. 21 Effect of angle of attack on the bandpassed pressure signal $(0.9 \le BPF \le 1.1)$ obtained at 10D in the plane of propeller rotation.

one order lower than at J = 0.60, which agrees with the previously observed lower loading and thickness noise for the former condition.

At $\alpha_{\infty}=10\,$ deg, the peak amplitude of the pressure signal of the thickness noise shows a slight variation with the azimuth as a consequence of the varying tip Mach number due to the crossflow, particularly evident for J=0.60 in Fig. 21a. Removing the crossflow component confirmed this, resulting in similar and almost constant thickness noise peak amplitudes at both α_{∞} values. The variation in the peak amplitude of the pressure signal of the loading noise at $\alpha_{\infty}=10\,$ deg is dominated by the unsteady blade loading effect for both J=0.60 and 1.10. Therefore, this variation directly corresponds to the variation in the blade loading seen in Fig. 14 with a shift of 90 deg as the loading noise is radiated in the perpendicular direction.

In addition to the variation in the peak amplitude of the pressure signal of the loading noise with the azimuth, the phase difference between the loading and thickness noise signals also varies at a nonzero angle of attack as shown in Fig. 21c. At $\alpha_{\infty}=0$ deg, the loading noise signal is 94 deg ahead of the thickness noise signal at the positive thrust condition (J=0.60) with negligible variations in the phase difference with the azimuthal position. On the other hand, the loading noise signal lags behind the thickness noise signal by approximately 102 deg in the negative thrust condition (J=1.10).

However, a nonzero α_{∞} introduces ϕ -dependent variations in the phase difference, irrespective of the thrust condition. For J=0.60, the phase difference increases between 0 deg $\leq \phi \leq 60$ deg, reaching a maximum phase difference of 133 deg at $\phi=60$ deg, and then starts to decrease between 60 deg $\leq \phi \leq 300$ deg, reaching a minimum phase difference of 55 deg at $\phi=300$ deg, and then it increases again. For the negative thrust condition, the phase difference between the loading and thickness noise signals decreases from -96 deg at $\phi=0$ deg to -172 deg at $\phi=150$ deg. The phase difference between the loading and thickness noise signals decreases beyond -180 deg for $\phi>150$ deg. It is shown as a positive phase difference by adding the 360 deg to the phase difference values due to the cyclic nature of the effect of the phase difference on the total noise. The phase difference between the

loading and thickness noise signals decreases from 179 deg at $\phi =$ 165 deg to -96 deg at $\phi =$ 360 deg. As the pressure signals of the loading and thickness noise are nearly out of phase for 120 deg $\leq \phi \leq$ 210 deg for the negative thrust condition, their sum results in a lower total noise level compared to when they are in phase or partially in phase at other azimuthal positions as seen in Fig. 19d.

These results show that, at nonzero angles of attack, two key factors influence the azimuthal variation in total noise: changes in peak amplitude and the changing phase difference between loading and thickness noise over the azimuth. The thickness noise signal remains nearly constant over the azimuth. The key physical phenomenon driving both the peak amplitude change and the phase difference variation is the varying blade loading over the azimuth. The variation in phase difference between thickness and loading noise presents a potential new parameter for propeller noise optimization, potentially allowing for reduced noise without compromising aerodynamic performance. Further research using the analytical solution of the FWH analogy is necessary to validate these findings.

B. Noise Directivity in Plane Along Propeller Axis

1. Positive Thrust Condition (J = 0.60)

Figure 22 illustrates the noise directivity along the propeller axis for the positive thrust condition (J=0.60). As thickness noise is a tonal noise source, it mainly radiates in the propeller plane (69 dB) and has zero contribution along the propeller axis, as seen in Fig. 22a. On the other hand, the loading noise has both broadband and tonal noise components, leading to a noise level of up to 61 dB along the propeller axis and 71 dB in the propeller plane. This is also evident in the noise directivity of the first BPF in Fig. 22c, where the tonal noise mainly propagates in the propeller plane, resulting in a total noise level of 74 dB at $\theta=90$ deg, compared to the noise level of 31–32 dB along the propeller axis.

While the noise directivity is symmetric around the propeller axis at 0 deg angle of attack (as expected), the same is not true at the

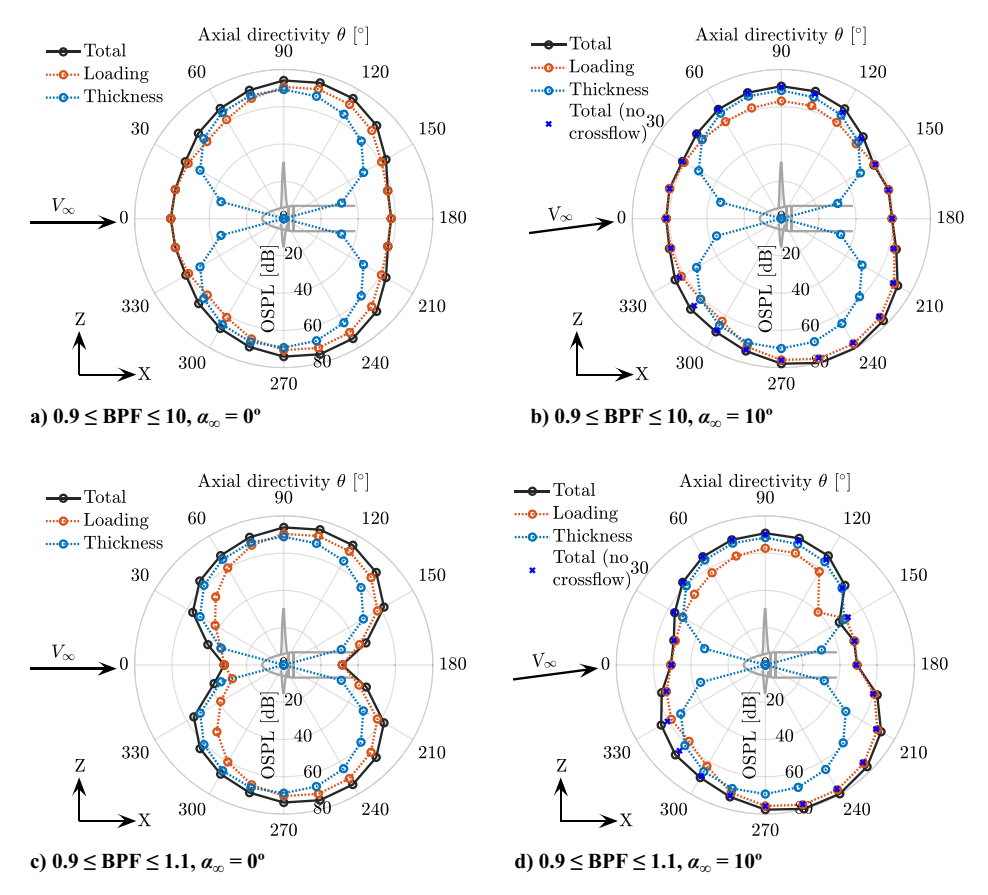


Fig. 22 Effect of angle of attack on the noise directivity along the propeller axis at the positive thrust condition (J = 0.60).

10 deg angle of attack. For the positive thrust condition, the total noise increases in the region where the propeller is tilted away and vice versa, as shown in Fig. 22b, which agrees with the trends seen in Sec. V.A.1. The change in the noise directivity is mainly driven by changes in the loading noise at the first BPF, as observed in Figs. 22b and 22d. The maximum change in the total noise is up to ± 8 dB at $\theta = 210$ deg and 135 deg, respectively, due to the significant change in the loading noise. As a result, the thickness noise becomes the dominant source of noise for 45 deg $\leq \theta \leq$ 135 deg in Figs. 22b and 22d.

Although the tonal noise changes significantly with the angle of attack, the broadband noise remains almost constant. This can be observed from the PSD plots shown in Fig. 23. There is no tonal noise at 0 deg angle of attack (as expected), but tonal peaks appear, albeit small, at $\alpha_{\infty}=10\,$ deg. It is important to acknowledge that the peaks at 1/3 and 1/6 BPF likely stem from numerical artifacts due to slight variations in blade loading across propeller blades, as

mentioned at the start of this section. Despite these numerical artifacts, a tonal peak is visible at the first BPF for the 10 deg AOA case compared to the 0 deg AOA case. Therefore, unsteady blade loading leads to the propagation of noise along the propeller axis, which is in agreement with the literature [41,43].

Similar to the previous Sec. V.A.1, the noise without the convective effect of the crossflow velocity component (blue-cross markers) shows similar trends as the noise with the convective effect of the crossflow velocity (Figs. 22b and 22d). Therefore, the asymmetric modulation of the noise sources is also irrelevant in the plane perpendicular to the plane of rotation.

2. Negative Thrust Condition (J = 1.10)

Figure 24 shows the noise directivity in the plane aligned with the propeller axis for the negative thrust condition (J = 1.10). As previously mentioned in Sec. V.A.2, the thickness noise is significantly reduced at J = 1.10 compared to J = 0.60, making the loading noise

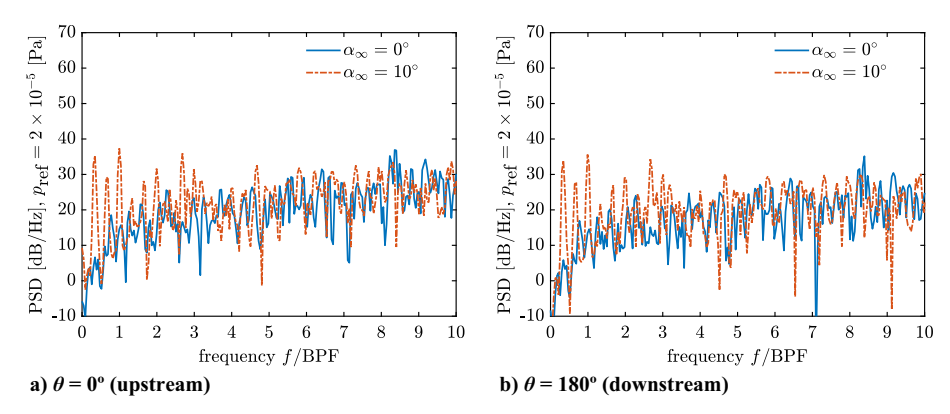


Fig. 23 Power spectrum density of the pressure signal obtained at virtual microphones located along the propeller axis at the positive thrust condition (J = 0.60).

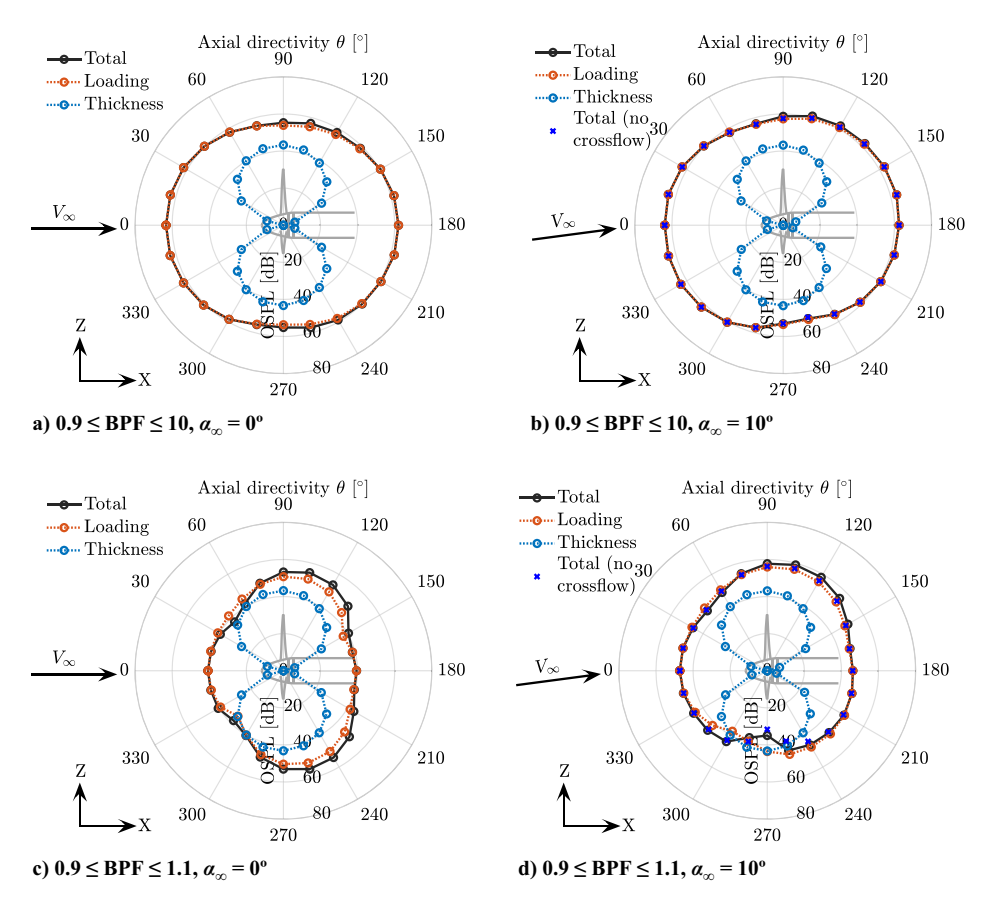


Fig. 24 Effect of angle of attack on the noise directivity along the propeller axis at the negative thrust condition (J = 1.10).

the dominant source of noise at both 0 deg and 10 deg angle of attack. The loading noise is higher along the propeller axis (63 dB at $\theta = 0$ deg and 62 dB at 180 deg) than in the propeller plane (54 dB at $\theta = 90$ deg and 270 deg), as shown in Fig. 24a. This is a consequence of significant broadband noise in the negative thrust condition due to extensive flow separation around the propeller blades. The reduced tonal noise compared to the positive thrust condition is partially due to the reduced absolute loading and reduced tip Mach number but also due to the change in the loading distribution along the blade span. Again, the noise directivity at 0 deg angle of attack is symmetric around the propeller axis as expected.

The directivity of noise at the first harmonic at 0 deg angle of attack (Fig. 24c) shows a significant noise level along the propeller axis (41 dB) due to the presence of broadband noise between $0.9 \le BPF \le 1.1$, as can be seen in the PSD plots in Fig. 25. The increased broadband contribution also results in some differences in the noise directivity above and below the propeller axis. Interestingly, the directivity at the first BPF shows destructive interference

between loading and thickness noise at $0 \, \deg < \theta < 75 \, \deg$, resulting in lower total noise at these axial directivity angles. This is expected to be the consequence of the same mechanism explained earlier in Sec. V.A.3.

At the 10 deg angle of attack, the directivity of noise is significantly altered with respect to the 0 deg AOA case, as can be seen in Fig. 24. The loading noise is increased up to 4 dB between 90 deg $\leq \theta \leq$ 180 deg and reduced up to 3 dB between 180 deg $\leq \theta \leq$ 270 deg compared to 0° angle of attack, as shown in Fig. 24b. These changes in the noise levels are opposite to the trends seen for J=0.60. As explained before in Sec. V.A.2, the differences in the noise directivity between negative and positive thrust conditions at nonzero angles of attack are the consequence of different variations in the absolute blade loading over the advancing and retreating sides (Fig. 14). Like all previous results, the total noise without convection effects shows identical results as the total noise with convection effects, indicating that the dominant mechanism responsible for changes in noise directivity at the 10 deg angle of attack is unsteady loading.

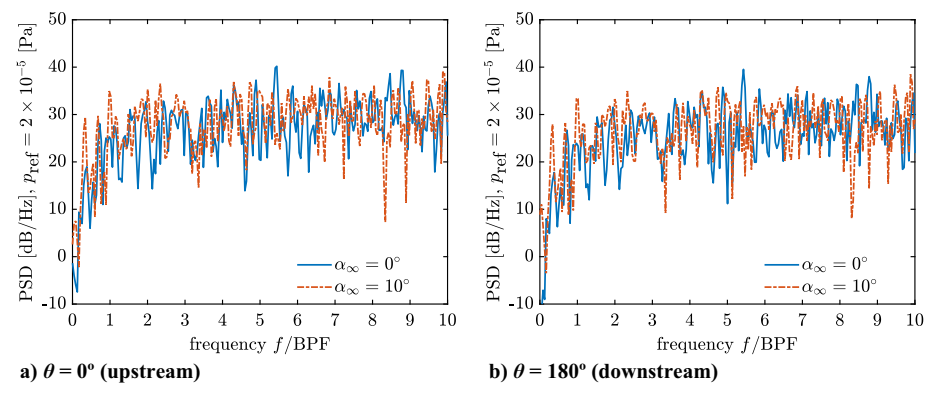


Fig. 25 Power spectrum density of the pressure signal obtained at virtual microphones located along the propeller axis at the negative thrust condition (J = 1.10).

The directivity of loading noise at the first BPF (Fig. 24d) also shows similar changes with the change in the angle of attack. However, an interesting change can be seen in the interference of the loading and thickness noise. In addition to the observed destructive interference between loading and thickness noise for 0 deg < θ < 75 deg at 0 deg angle of attack, there is also destructive interference for 210 deg $\leq \theta$ < 300 deg at 10 deg angle of attack, which reduces total noise in the lower part of the plane. This phenomenon has been explained earlier in Sec. V.A.3.

Contrary to expectations, the broadband noise stays almost constant with the change of angle of attack. This can also be seen from PSD plots shown in Fig. 25. Unlike the positive thrust case, no clear tonal peaks are observed along the propeller axis at the 10 deg angle of attack due to the lower tonal noise compared to the broadband noise in this case.

VI. Conclusions

This study employed a lattice-Boltzmann method coupled with a very large-eddy model to investigate the impact of a nonzero AOA on aerodynamics and far-field noise characteristics of an isolated propeller operating at positive and negative thrust conditions. The simulations were validated against experimental data by comparing the relative change in propeller performance at the 10 deg angle of attack with respect to the 0 deg angle of attack case.

At nonzero AOA, the direction of the normal and side forces remained unchanged in the propeller axis aligned reference frame, while thrust and torque directions reversed between positive and negative thrust regimes. The combined effects of the positive thrust and positive normal force resulted in a significant positive lift $0.30T_{C_m}$ in the positive thrust condition. In contrast, the positive normal force counters the negative thrust component in the negative thrust condition, resulting in a small negative lift $0.05T_{C_\infty}$. Along the freestream direction, the propeller efficiency $\eta_{p_{\infty}}$ remained nearly unaffected by AOA in positive thrust conditions. Given that operating the propeller at a positive thrust and a positive AOA generates positive lift without affecting $\eta_{p_{\infty}}$, installing the propeller at such an AOA may prove beneficial at the aircraft level. In contrast, such an installation would yield a lower harvested energy than the equivalent operation at 0 deg AOA and the generation of a negative lift when operated at negative thrust.

At a negative thrust condition with a 10 deg AOA, a dynamic stall was observed on the inboard sections of the propeller blade, with flow attaching on the advancing side and separating on the retreating side. Meanwhile, the outboard sections, already stalled at the 0 deg AOA, undergo changes in the extent of separation with azimuthal position (with a noticeable increase in broadband fluctuations on the retreating side). Near the blade tip (r/R = 0.90), the periodic fluctuations deviate from a sinusoidal pattern due to the operation of blade sections in a deep stall region, where broadband fluctuations in the local thrust coefficient ($\pm 7\%$ of the mean thrust level) are comparable in magnitude to the periodic variations (-10% to +7% of the mean thrust level).

The operation at a nonzero AOA results in an asymmetry in the slipstream as a result of sinusoidal variation in the geometric AOA over the azimuth. The operation of the propeller at 10 deg AOA results in a higher dynamic pressure on the advancing side compared to the retreating side for both positive and negative thrust conditions. A wing immersed in such propeller slipstream experiences distinct effects depending on the thrust condition and AOA. In positive thrust conditions, when the propeller and wing have the same sign of AOA (both positive or both negative), differences in slipstream dynamic pressure between the advancing and retreating sides tend to reduce the differences in lift increase between the upgoing and downgoing blade sides compared to the 0 deg case. In negative thrust conditions, when the propeller and wing have the same sign of AOA, differences in slipstream dynamic pressure between the advancing and retreating sides amplify the differences in lift reduction between the upgoing and downgoing blade sides compared to the 0 deg case, with a greater reduction in lift on the upgoing blade side.

The changes in the propeller blade loading lead to changes in the far-field aeroacoustic performance. In the plane of propeller rotation, the first blade passing frequency exhibits increased noise (up to 5 dB) in the region away from the tilt direction and decreased noise (up to 8 dB) toward the tilt direction for the positive thrust condition. This trend reverses in the negative thrust case, with increased noise toward the tilt direction (up to 6 dB) and decreased noise away from it (up to 12 dB) at the first BPF. These opposing trends are a direct consequence of the opposite changes in absolute blade loading caused by the AOA. In the plane along the propeller axis (in which the freestream is tilted to change AOA), noise levels are higher along the propeller axis (62-63 dB) than in the plane of rotation (54-59 dB) in the negative thrust condition for both angles of attack (0 deg and 10 deg). In contrast, positive thrust exhibits lower noise levels along the propeller axis (58-62 dB) compared to the plane of rotation (71-78 dB). This results from higher broadband noise and lower tonal noise in the negative thrust condition than in the positive thrust condition.

Furthermore, in the negative thrust condition, destructive interference between thickness noise and loading noise reduces the total noise in specific regions: 120 deg < ϕ < 210 deg in the propeller plane and 210 deg $\leq \theta$ < 300 deg in the plane along the propeller axis. This destructive interference results from the approximately \pm 180 deg phase difference between the loading and thickness noise signal at the specified locations. The phase difference between the loading and the thickness noise signals varies over the azimuth for the nonzero AOA as a consequence of the varying blade loading over the azimuth. The variation in phase difference between thickness and loading noise presents a potential new parameter for propeller noise optimisation, potentially allowing for reduced noise without compromising aerodynamic performance. Further research using the analytical solution of the FWH analogy is necessary to validate these findings.

The novel results presented in this chapter provide valuable insights into the aerodynamic and aeroacoustic behavior of conventional propellers operating in positive and negative thrust conditions at a nonzero AOA. This is an important step toward enhancing the understanding of the complex propeller—wing interactions that occur under such conditions.

Acknowledgments

The research leading to these results is part of the FUTPRINT50 project. This project has received funding from the European Union's Horizon 2020 Research and Innovation programme under Grant Agreement Number 875551. This work made use of the Dutch national e-infrastructure with the support of the SURF Cooperative using grant number EINF-2733. The authors would like to thank Robert Nederlof for providing the experimental data for the validation of the simulations and Fernanda do Nascimento Monteiro for her efforts in providing insights into aeroacoustic results.

References

- Veldhuis, L. L. M., "Propeller Wing Aerodynamic Interference," Ph.D. Dissertation, Delft Univ. of Technology, The Netherlands, 2005, http:// resolver.tudelft.nl/uuid:8ffbde9c-b483-40de-90e0-97095202fbe3.
- [2] Hartman, E. P., "Negative Thrust and Torque Characteristics of an Adjustable-Pitch Metal Propeller," *Annual Report-National Advisory Committee for Aeronautics*. Vol. 19, 1933, p. 421, http://hdl.handle.net/2060/19930091538.
- [3] Hedrick, W. S., and Douglass, W. M., "An Experimental Investigation of the Thrust and Torque Produced by Propellers Used as Aerodynamic Brakes," National Advisory Committee for Aeronautics WR-A-27, 1944, http://hdl.handle.net/2060/19930093338.
- [4] Thomas, J. L., and Hansman, R. J., "Community Noise Reduction Assessment of Using Windmilling Drag on Approach by Hybrid Electric Aircraft," AIAA Aviation 2020 Forum, AIAA Paper 2020-2877, June 2020. https://doi.org/10.2514/6.2020-2877
- [5] Barnes, J. P., "Regenerative Electric Flight: Synergy and Integration of Dual-Role Machines," 53rd AIAA Aerospace Sciences Meeting, AIAA

- Paper 2015-1302, Jan. 2015. https://doi.org/10.2514/6.2015-1302
- [6] Eržen, D., Andrejašič, M., Lapuh, R., Tomažič, J., Gorup, Č., and Kosel, T., "An Optimal Propeller Design for In-Flight Power Recuperation on an Electric Aircraft," 2018 Aviation Technology, Integration, and Operations Conference, AIAA Paper 2018-3206, June 2018. https://doi.org/10.2514/6.2018-3206
- [7] Goyal, J., Sinnige, T., Avallone, F., and Ferreira, C., "Aerodynamic and Aeroacoustic Characteristics of an Isolated Propeller at Positive and Negative Thrust," AIAA Aviation 2021 Forum, AIAA Paper 2021-2187, June 2021. https://doi.org/10.2514/6.2021-2187
- [8] Nederlof, R., Ragni, D., and Sinnige, T., "Experimental Investigation of the Aerodynamic Performance of a Propeller at Positive and Negative Thrust and Power," AIAA AVIATION 2022 Forum, AIAA Paper 2022-3893, June 2022. https://doi.org/10.2514/6.2022-3893
- [9] Nederlof, R., Ragni, D., and Sinnige, T., "Energy-Harvesting Performance of an Aircraft Propeller" (Under Review).
- [10] Goyal, J., Avallone, F., and Sinnige, T., "Isolated Propeller Aeroacoustics at Positive and Negative Thrust," *Aerospace Science and Technology*, Vol. 147, April 2024, Paper 109021. https://doi.org/10.1016/j.ast.2024.109021
- [11] Sinnige, T., Stokkermans, T. C. A., van Arnhem, N., and Veldhuis, L. L. M., "Aerodynamic Performance of a Wingtip-Mounted Tractor Propeller Configuration in Windmilling and Energy-Harvesting Conditions," AIAA Aviation 2019 Forum, AIAA Paper 2019-3033, June 2019. https://doi.org/10.2514/6.2019-3033
- [12] Sinnige, T., Nederlof, R., and van Arnhem, N., "Aerodynamic Performance of Wingtip-Mounted Propellers in Tractor and Pusher Configuration," AIAA Aviation 2021 Forum, AIAA Paper 2021-2511, 2021. https://doi.org/10.2514/6.2021-2511
- [13] Farassat, F., and Succi, G. P., "A Review of Propeller Discrete Frequency Noise Prediction Technology with Emphasis on Two Current Methods for Time Domain Calculations," *Journal of Sound and Vibration*, Vol. 71, No. 3, 1980, pp. 399–419. https://doi.org/10.1016/0022-460X(80)90422-8
- [14] Casalino, D., Hazir, A., and Mann, A., "Turbofan Broadband Noise Prediction Using the Lattice Boltzmann Method," *AIAA Journal*, Vol. 56, No. 2, 2018, pp. 609–628. https://doi.org/10.2514/1.J055674
- [15] Gonzalez-Martino, I., and Casalino, D., "Fan Tonal and Broadband Noise Simulations at Transonic Operating Conditions Using Lattice-Boltzmann Methods," 2018 AIAA/CEAS Aeroacoustics Conference, AIAA Paper 2018-3919, 2018. https://doi.org/10.2514/6.2018-3919
- [16] Bres, G., Pérot, F., and Freed, D., "Properties of the Lattice Boltzmann Method for Acoustics," 15th AIAA/CEAS Aeroacoustics Conference (30th AIAA Aeroacoustics Conference), AIAA Paper 2009-3395, 2009. https://doi.org/10.2514/6.2009-3395
- [17] Marié, S., Ricot, D., and Sagaut, P., "Comparison Between Lattice Boltzmann Method and Navier–Stokes High Order Schemes for Computational Aeroacoustics," *Journal of Computational Physics*, Vol. 228, No. 4, 2009, pp. 1056–1070. https://doi.org/10.1016/j.jcp.2008.10.021
- [18] Succi, S., The Lattice Boltzmann Equation: for Fluid Dynamics and Beyond, Oxford Univ. Press, Oxford, 2001. https://doi.org/10.1063/1.1537916
- [19] Shan, X., Yuan, X.-F., and Chen, H., "Kinetic Theory Representation of Hydrodynamics: A Way Beyond the Navier–Stokes Equation," *Journal of Fluid Mechanics*, Vol. 550, No. -1, 2006, pp. 413–441. https://doi.org/10.1017/S0022112005008153
- [20] Chen, H., Zhang, R., and Gopalakrishnan, P., "Lattice Boltzmann Collision Operators Enforcing Isotropy and Galilean Invariance," Feb. 2017, https://patents.google.com/patent/CA2919062A1/en.
- [21] Chen, H., Chen, S., and Matthaeus, W. H., "Recovery of the Navier-Stokes Equations Using a Lattice-Gas Boltzmann Method," *Physical Review A*, Vol. 45, No. 8, 1992, Paper R5339. https://doi.org/10.1103/PhysRevA.45.R5339
- [22] Yakhot, V., and Orszag, S. A., "Renormalization Group Analysis of Turbulence. I. Basic Theory," *Journal of Scientific Computing*, Vol. 1, No. 1, 1986, pp. 3–51. https://doi.org/10.1007/BF01061452
- [23] Teixeira, C. M., "Incorporating Turbulence Models into the Lattice-Boltzmann Method," *International Journal of Modern Physics C*, Vol. 9, No. 08, 1998, pp. 1159–1175. https://doi.org/10.1142/S0129183198001060
- [24] Wilcox, D. C., *Turbulence Modelling for CFD*, 3rd ed., DCW Industries, La Canada CA, 2006, pp. 181–192.

[25] Launder, B. E., and Spalding, D. B., "The Numerical Computation of Turbulent Flows," *Computer Methods in Applied Mechanics and Engi*neering, Vol. 3, No. 2, 1974, pp. 269–289. https://doi.org/10.1016/0045-7825(74)90029-2

- [26] Avallone, F., van den Ende, L., Li, Q., Ragni, D., Casalino, D., Eitelberg, G., and Veldhuis, L., "Aerodynamic and Aeroacoustic Effects of Swirl Recovery Vanes Length," *Journal of Aircraft*, Vol. 56, No. 6, 2019, pp. 2223–2235. https://doi.org/10.2514/1.C035552
- [27] Casalino, D., "An Advanced Time Approach for Acoustic Analogy Predictions," *Journal of Sound and Vibration*, Vol. 261, No. 4, 2003, pp. 583–612. https://doi.org/10.1016/S0022-460X(02)00986-0
- [28] Turner, J. M., and Kim, J. W., "Quadrupole Noise Generated from a Low-Speed Aerofoil in Near-and Full-Stall Conditions," *Journal of Fluid Mechanics*, Vol. 936, Feb. 2022, Paper A34. https://doi.org/10.1017/jfm.2022.75
- [29] Goyal, J., Sinnige, T., Avallone, F., and Ferreira, C., "Benchmarking of Aerodynamic Models for Isolated Propellers Operating at Positive and Negative Thrust," *AIAA Journal*, Vol. 62, No. 10, 2024, pp. 3758– 3775. https://doi.org/10.2514/1.J064093
- [30] O'meara, M., and Mueller, T. J., "Laminar Separation Bubble Characteristics on an Airfoil at Low Reynolds Numbers," AIAA Journal, Vol. 25, No. 8, 1987, pp. 1033–1041. https://doi.org/10.2514/3.9739
- [31] Ol, M., McCauliffe, B., Hanff, E., Scholz, U., and Kähler, C., "Comparison of Laminar Separation Bubble Measurements on a Low Reynolds Number Airfoil in Three Facilities," 35th AIAA Fluid Dynamics Conference and Exhibit, AIAA Paper 2005-5149, 2005.
- https://doi.org/10.2514/6.2005-5149
 [32] Temmerman, L., and Leschziner, M. A., "Large Eddy Simulation of Separated Flow in a Streamwise Periodic Channel Constriction," 2nd Symposium on Turbulence and Shear Flow Phenomena, Begell House Inc., Danbury, CT, 2001, pp. 399–404. https://doi.org/10.1615/TSFP2.2300
- [33] Temmerman, L., Leschziner, M. A., Mellen, C. P., and Fröhlich, J., "Investigation of Wall-Function Approximations and Subgrid-Scale Models in Large Eddy Simulation of Separated Flow in a Channel with Streamwise Periodic Constrictions," *International Journal of Heat and Fluid Flow*, Vol. 24, No. 2, 2003, pp. 157–180. https://doi.org/10.1016/S0142-727X(02)00222-9
- [34] Barlow, J., Rae, W., and Pope, A., Low-Speed Wind Tunnel Testing, Wiley, Hoboken, NJ, 1999, pp. 368–375, 433–435.
- [35] DeLoach, R., "Improved Quality in Aerospace Testing Through the Modern Design of Experiments," 38th Aerospace Sciences Meeting and Exhibit, AIAA Paper 2000-0825, 2000. https://doi.org/10.2514/6.2000-825
- [36] von Karman, T. H., and Sears, W. R., "Airfoil Theory for Non-Uniform Motion," *Journal of the Aeronautical Sciences*, Vol. 5, No. 10, 1938, pp. 379–390. https://doi.org/10.2514/8.674
- [37] De Young, J., "Propeller at High Incidence," *Journal of Aircraft*, Vol. 2, No. 3, 1965, pp. 241–250. https://doi.org/10.2514/3.43646
- [38] Ortun, B., Boisard, R., and Gonzalez-Martino, I., "In-Plane Airloads of a Propeller with Inflow Angle: Prediction vs. Experiment," 30th AIAA Applied Aerodynamics Conference, AIAA Paper 2012-2778, 2012. https://doi.org/10.2514/6.2012-2778
- [39] van Arnhem, N., "Unconventional Propeller-Airframe Integration for Transport Aircraft Configurations," Ph.D. Thesis, Delft Univ. of Technology, Delft, The Netherlands, 2022. https://doi.org/10.4233/uuid:4d47b0db-1e6a-4f38-af95-aafd33c29402
- [40] Mani, R., "The Radiation of Sound from a Propeller at Angle of Attack," Proceedings of the Royal Society of London. Series A: Mathematical and Physical Sciences, Vol. 431, No. 1882, 1990, pp. 203–218. https://doi.org/10.1098/rspa.1990.0127
- [41] Romani, G., Grande, E., Avallone, F., Ragni, D., and Casalino, D., "Computational Study of Flow Incidence Effects on the Aeroacoustics of Low Blade-Tip Mach Number Propellers," *Aerospace Science and Technology*, Vol. 120, Jan. 2022, Paper 107275. https://doi.org/10.1016/j.ast.2021.107275
- [42] Carley, M., "The Structure of Wobbling Sound Fields," *Journal of Sound and Vibration*, Vol. 244, No. 1, 2001, pp. 1–19. https://doi.org/10.1006/jsvi.2000.3451
- [43] Hanson, D., "Sound from a Propeller at Angle of Attack: A New Theoretical Viewpoint," Proceedings of the Royal Society of London.

Series A: Mathematical and Physical Sciences, Vol. 449, No. 1936, 1995, pp. 315-328.

https://doi.org/10.1098/rspa.1995.0046

- [44] Block, P., "The Effects of Installation on Single-and Counter-Rotation Propeller Noise," 9th Aeroacoustics Conference, AIAA Paper 1984-2263,
 - https://doi.org/10.2514/6.1984-2263
- [45] Block, P., Experimental Study of the Effects of Installation on Singleand Counter-Rotation Propeller Noise, vol. 2541, National Aeronautics
- and Space Administration, Scientific and Technical Information Branch, NASA TP-2541, 1986, https://ntrs.nasa.gov/citations/ 19860016690.
- [46] Woodward, R., "Measured Noise of a Scale Model High Speed Propeller at Simulated Takeoff/Approach Conditions," 25th AIAA Aerospace Sciences Meeting, AIAA Paper 1987-526, 1987.

A. Gopalarathnam Associate Editor